

**Journal of Geophysical Research: Solid Earth****RESEARCH ARTICLE**

10.1002/2014JB011638

**Key Points:**

- Three-dimensional radially anisotropic model beneath East Asia
- $V_p$ ,  $V_{SH}$ , and  $V_{SV}$  are independently constrained with the same data set
- Improved correlations with surface tectonic units compared to previous models

**Supporting Information:**

- Figures S1–S12

**Correspondence to:**

M. Chen,  
min.chen@rice.edu

**Citation:**

Chen, M., F. Niu, Q. Liu, J. Tromp, and X. Zheng (2015), Multiparameter adjoint tomography of the crust and upper mantle beneath East Asia: 1. Model construction and comparisons, *J. Geophys. Res. Solid Earth*, 120, 1762–1786, doi:10.1002/2014JB011638.

Received 23 SEP 2014

Accepted 27 JAN 2015

Accepted article online 31 JAN 2015

Published online 30 MAR 2015

**Multiparameter adjoint tomography of the crust and upper mantle beneath East Asia: 1. Model construction and comparisons****Min Chen<sup>1</sup>, Fenglin Niu<sup>1,2</sup>, Qinya Liu<sup>3</sup>, Jeroen Tromp<sup>4,5</sup>, and Xiufen Zheng<sup>6</sup>**<sup>1</sup>Department of Earth Science, Rice University, Houston, Texas, USA, <sup>2</sup>State Key Laboratory of Petroleum Resource and Prospecting, and Unconventional Natural Gas Institute, China University of Petroleum, Beijing, China, <sup>3</sup>Department of Physics, University of Toronto, Toronto, Ontario, Canada, <sup>4</sup>Department of Geosciences, Princeton University, Princeton, New Jersey, USA, <sup>5</sup>Program in Applied and Computational Mathematics, Princeton University, Princeton, New Jersey, USA,<sup>6</sup>Institute of Geophysics, China Earthquake Administration, Beijing, China

**Abstract** We present a 3-D radially anisotropic model of the crust and mantle beneath East Asia down to 900 km depth. Adjoint tomography based on a spectral element method is applied to a phenomenal data set comprising 1.7 million frequency-dependent traveltimes from waveforms of 227 earthquakes recorded by 1869 stations. Compressional wave speeds are independently constrained and simultaneously inverted along with shear wave speeds ( $V_{SH}$  and  $V_{SV}$ ) using the same waveform data set with comparable resolution. After 20 iterations, the new model (named EARA2014) exhibits sharp and detailed wave speed anomalies with improved correlations with surface tectonic units compared to previous models. In the upper 100 km, high wave speed (high-V) anomalies correlate very well with the Junggar and Tarim Basins, the Ordos Block, and the Yangtze Platform, while strong low wave speed (low-V) anomalies coincide with the Qiangtang Block, the Songpan Ganzi Fold Belt, the Chuandian Block, the Altay-Sayan Mountain Range, and the back-arc basins along the Pacific and Philippine Sea Plate margins. At greater depths, narrow high-V anomalies correspond to major subduction zones and broad high-V anomalies to cratonic roots in the upper mantle and fragmented slabs in the mantle transition zone. In particular, EARA2014 reveals a strong high-V structure beneath Tibet, appearing below 100 km depth and extending to the bottom of the mantle transition zone, and laterally spanning across the Lhasa and Qiangtang Blocks. In this paper we emphasize technical aspects of the model construction and provide a general discussion through comparisons.

**1. Introduction**

Our East Asia study region (Figure 1) is bordered by the Himalaya Main Boundary Thrust and the Tianshan Mountain Range in the west, the Japan and Izu-Bonin-Mariana Trenches in the east, Lake Baikal in the north, and Malaysia and the Philippines in the south. This region has drawn much attention due to its complex tectonic history involving continent-continent collision, oceanic plate subduction, various types of basin formation, intracontinental rifting, and intraplate volcanism and magmatism. The main driving forces of these tectonic activities have been attributed to the India-Eurasia collision in the west [Allégre *et al.*, 1984; Tapponnier *et al.*, 1986; Dewey *et al.*, 1989; Burchfiel and Royden, 1991; Yin and Harrison, 2000] and subduction of the Pacific Plate beneath Eurasia in the east [Northrup *et al.*, 1995; Honza and Fujioka, 2004; Schellart and Lister, 2005].

The southwest margin and neighboring regions have undergone massive compression due to the India-Eurasia collision. This continent-continent collision created not only the highest mountain system on earth but also the most elevated and largest plateau: the Tibetan Plateau with an average elevation of 4.5 km and an area of 2.5 million square kilometers. Convergence of the Indian and Eurasian plates, besides being absorbed by the Himalayan orogeny and uplift of the Tibetan Plateau, was also partially accommodated by very large sinistral and dextral fault systems, such as the Karakorum, Kunlun, and Altyn-Tagh Faults [Tapponnier *et al.*, 1986]. The other significant topographic features resulting from this collision are numerous flexural basins, such as the Tarim, Junggar, and Qaidam Basins [Watson *et al.*, 1987]. Previous seismic imaging studies have revealed high wave speed (high-V) Indian Plate subducting beneath the Tibetan plateau and low wave speed (low-V) zones residing in the sub-Tibetan lower crust and uppermost mantle [Brandon and Romanowicz, 1986; Bourjot and Romanowicz, 1992; Tilman *et al.*, 2003; Priestley and McKenzie, 2006; Li *et al.*, 2008; Yao *et al.*, 2010; Panning

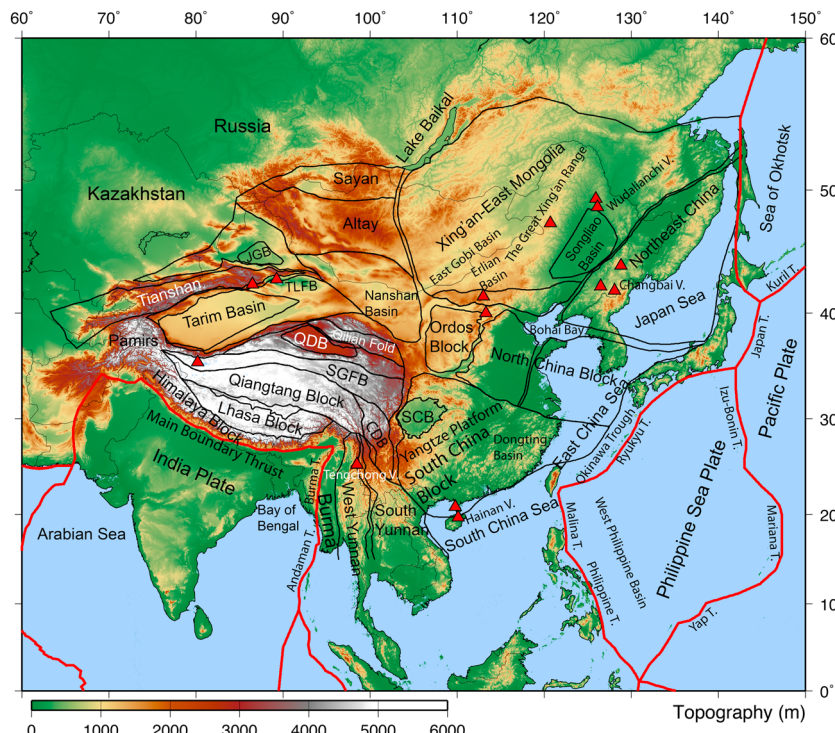


**Figure 1.** Tectonic and topographic map of Southeast Asia. Red triangles mark active volcanoes. Dark lines define the main tectonic units and basins. Abbreviations are as follows: CDB, Chuandian Block; JGB, Junggar Basin; QDB, Qaidam Basin; SCB, Sichuan Basin; TLFB, Tulufan Basin; SGFB, Songpan Ganzi Fold Belt. Tectonic unit boundaries are also drawn in later depth view tomographic maps in bold grey lines for reference. Red bold lines delineate plate boundaries from NUVEL-1 [DeMets *et al.*, 1990].

*et al.*, 2012; Yang *et al.*, 2012]. However, the northern extent of Indian Plate subduction and whether or not uplift of the Tibetan Plateau is due to a low-V crustal weak zone are still heatedly debated topics, mainly due to limited seismic imaging resolution.

The eastern margin of East Asia experienced widespread extension due to subduction of the Pacific plate and slab rollback. Asthenospheric upwelling and the interplay of mantle flow with lithosphere-asthenosphere boundary topography play an important role in building a large number of continental rift systems and marginal sea basins since the Late Mesozoic [Ren *et al.*, 2002]. Controversies exist regarding the origin of the Altay-Sayan and Baikal rift systems, namely, whether they are due to a mantle plume [Khain, 1990; Windley and Allen, 1993; Cunningham, 1998; Barry *et al.*, 2003; Zorin *et al.*, 2006; Tiberti *et al.*, 2008] and/or lithospheric processes [Cunningham, 2001; Petit *et al.*, 2002; Barry *et al.*, 2003; Anderson, 2005; Hunt *et al.*, 2012]. The origin of Changbai volcanism is also debated: competing hypotheses include the big mantle wedge model [Lei and Zhao, 2005; Zhao *et al.*, 2009], subduction-triggered magmatic pulses [Faccenna *et al.*, 2010], and subduction-induced upwelling with return flow of subslab hot mantle material through a “stagnant slab gap” [Tang *et al.*, 2014].

Previous seismic traveltimes inversions based on ray, paraxial kernel, or normal mode-based theories have shed important light on how the interior beneath East Asia influences surface tectonics [Friederich, 2003; Huang and Zhao, 2006; Kustowski *et al.*, 2008b; Li and van der Hilst, 2010; Obrebski *et al.*, 2012; Panning *et al.*, 2012; Wei *et al.*, 2012; Zhao *et al.*, 2012]. Specifically, tracing remnants of ancient lithosphere in seismic images helped to distinguish different mechanisms for the Himalayan orogeny, uplift of the Tibetan Plateau, and intraplate volcanism. These seismic images also provide the current slab morphology above, inside, and below the transition zone. Besides narrow high-V slab features above the mantle transition zone beneath the Japan, Ryukyu, Philippine, and Himalayan Arcs, high-V anomalies beneath the Yangtze Platform and the Ordos Block are also evident, implying the presence of a thermally and maybe compositionally distinct continental roots beneath these cratons. Low-V anomalies correlate well with the active Changbai and

Wudalianchi intraplate volcanoes in northeast China and the Tengchong volcano in southwest China. Pronounced deep slow anomalies are located beneath Hainan and the South China Sea. Despite all the similar features on large scales, differences exist among these tomographic results due to different methodologies and/or data sets. For example, compared to shear wave speed anomalies from surface wave and shear wave studies beneath the eastern Tibetan Plateau [Lebedev and van der Hilst, 2008; Obrebski et al., 2012], which indicate high-V anomalies in the 100 km–200 km depth range, a compressional wave study [Li et al., 2008] suggests low-V anomalies instead. Differences also exist among various compressional wave tomographic models. The crust and upper mantle beneath the Tarim and Junggar Basins, between their basements and 200 km depth, appear as high-V anomalies in the compressional wave speed tomography study by Huang and Zhao [2006] but as relatively low-V anomalies in the study by Li and van der Hilst [2010]. Discrepancies among different compressional wave speed and shear wave speed models limit further interpretation.

Given the current state of tomography of East Asia, there are several notable advantages in using adjoint tomography [Tromp et al., 2005; Liu and Tromp, 2006, 2008; Chen et al., 2007; Tape et al., 2007, 2009, 2010; Fichtner et al., 2009, 2010; Zhu et al., 2012a, 2012b] to obtain more coherent and robust images of both compressional and shear wave speeds. (1) Adjoint tomography eliminates crustal corrections, which are required in traditional body wave and surface wave tomography. Instead, a 3-D crustal model is embedded in the initial model and gets updated at each iteration. (2) All usable segments in seismograms, including body and surface waves, are used in the inversion for a more compatible model that improves the overall synthetic waveform fit to the data. (3) Simultaneously inverting for multiple parameters of a radially anisotropic model provides more constraints on the nature of seismic anomalies. (4) An iterative gradient-based minimization scheme supplemented by more accurate finite-frequency kernels better recovers wave speed anomaly amplitudes. (5) Accurate forward waveform modeling is a natural component of the iterative inversion process.

In this paper we present the first adjoint tomography model of East Asia, which describes 3-D crust and upper mantle structure in terms of isotropic shear wave speed  $V_S$ , isotropic compressional wave speed  $V_P$ , and radial anisotropy  $\xi = (V_{SH} - V_{SV})/V_S$  (where  $V_{SH}$  and  $V_{SV}$  denote the wave speeds of horizontally traveling and horizontally and vertically polarized shear waves, respectively). Our model contains high-V slab features at greater depths consistent with previous studies but exhibits improved correlations between wave speed anomalies in the upper 100 km and surface tectonic units. Here we focus on presenting the technical details of model construction, including discussions of the data set, inversion method, and model quality. We also provide a very general discussion of the model based on comparisons with existing models. The second part of this study, a detailed model interpretation guided by radial anisotropy and the  $V_P/V_S$  ratio to probe rheological and compositional properties that affect seismic waveforms, will be presented in a subsequent publication.

## 2. Data and Method

We use three-component waveforms recorded by 1869 stations from F-net, CEArray [Zheng et al., 2009], NECESSArray, INDEPTH IV Array, and other regional and global seismic Networks (Figure 2). The large majority of seismic sensors are broadband (50 Hz to 60 s or 120 s). Only a small percentage of the sensors are ultrabroadband (50 Hz to 360 s) and short-period borehole installations (50 Hz to 1 s or 2 s). The station distribution map indicates a phenomenal data coverage, especially to the east of 90°E within China. From the global centroid moment tensor (CMT) solution database, we select 227 earthquakes ( $M_w = 5–7$ ) (black and red beach balls in Figure 2) that have high signal-to-noise-ratio records for both source and structural inversions, and an extra set of 39 earthquakes not used in the inversions for model validation (green beach balls in Figure 2). In order to increase wavefield coverage for the structural inversion, we try to include earthquakes (black and red beach balls in Figure 2) located in all azimuths with respect to CEArray stations, which compose the main component of our data set. However, due to limited data availability, the chosen earthquakes are mainly distributed in seismogenic zones associated with active subduction or tectonic deformation and faulting, such as the subduction zones of Japan, Izu-Bonin, Mariana, Ryukyu, Philippine, Himalaya, and Burma. Only a few earthquakes are located to the west and north of China, close to Pamir, Tianshan, and Lake Baikal. Several earthquakes occurred inland in the Longmenshan fault zone, where the 2008 Wenchuan earthquake ruptured.

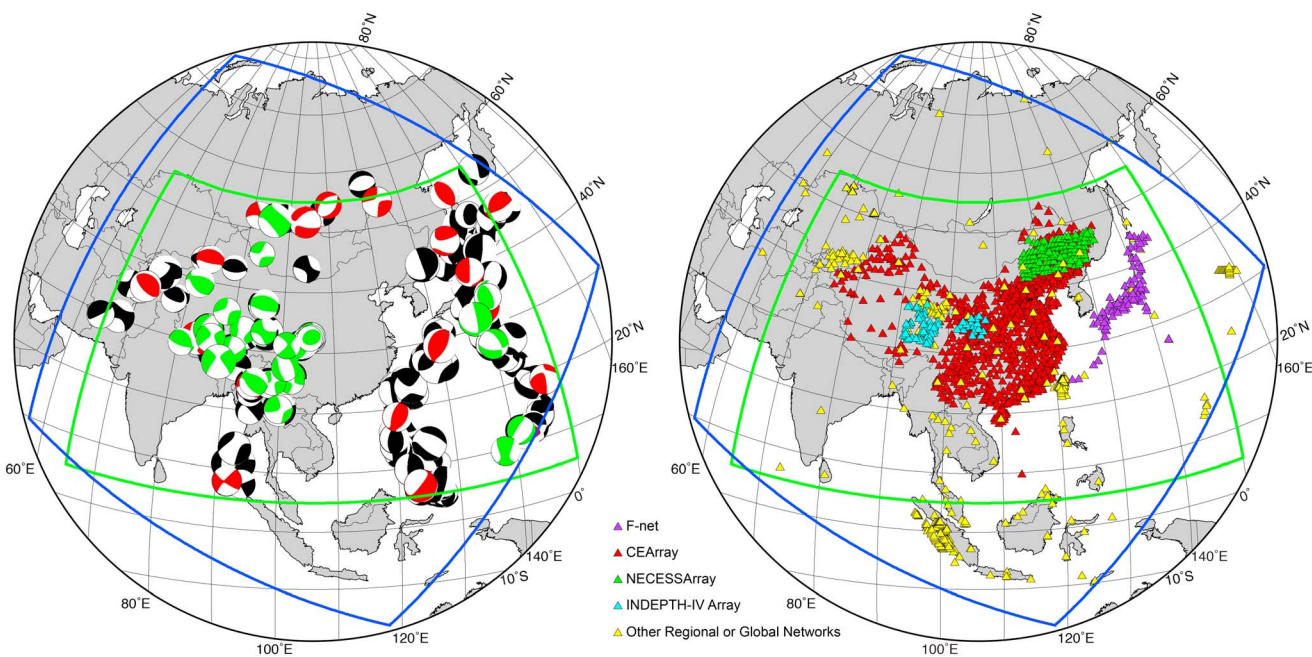


**Figure 2.** Map of earthquakes (beach balls) and stations (triangles) used in this study. Colored triangles represent different arrays or networks of stations. Black and red beach balls indicate a total of 227 earthquakes involved in the source and structural inversions. Red beach balls mark a subset of 20 earthquakes used in the conjugate gradient line search for updating models. Green beach balls indicate the extra 39 earthquakes used as an independent data set for model validation. The blue box indicates the simulation model domain, and the green box defines the region for showing maps at constant depths in Figures 6–12 and Figures S7, S8, S11, and S12 in the supporting information.

Our inversion involves reinverting source parameters within the initial 3-D model and iteratively refining the model based on finite-frequency kernels. A radially anisotropic model requires six parameters: the mass density  $\rho$ , the wave speed of horizontally traveling compressional waves  $V_{\text{PH}}$ , the wave speed of vertically traveling compressional waves  $V_{\text{PV}}$ , the wave speed of horizontally traveling and horizontally polarized shear waves  $V_{\text{SH}}$ , the wave speed of horizontally traveling and vertically polarized shear waves  $V_{\text{SV}}$ , and the dimensionless parameter  $\eta$  (which affects wave propagation at intermediate incidence angles). However, our data set cannot resolve  $V_{\text{PH}}$  and  $V_{\text{PV}}$  independently, so we reduce the number of parameters by one by focusing on the isotropic bulk sound speed  $V_c$ . Additionally, we cannot resolve mass density,  $\rho$ , which we scale to isotropic shear wave speed perturbations based on a factor of 0.33 [Anderson, 1987]. Due to a tradeoff between isotropic 3-D heterogeneity and radial anisotropy inside the crust and a lack of data coverage below the mantle transition zone, we use an isotropic parameterization in the crust and in the mantle below the transition zone, and a radially anisotropic parameterization between the Moho and the 650 km discontinuity. Changes in the frequency-dependent traveltimes misfit,  $\delta\chi$ , can thus be expressed in terms of the four parameters  $V_c$ ,  $V_{\text{SH}}$ ,  $V_{\text{SV}}$ , and  $\eta$  as [Zhu *et al.*, 2012b]

$$\delta\chi = \int (K_{V_c} \delta \ln V_c + K_{V_{\text{SH}}} \delta \ln V_{\text{SH}} + K_{V_{\text{SV}}} \delta \ln V_{\text{SV}} + K_\eta \delta \ln \eta) d^3x, \quad (1)$$

where the kernels  $K_{V_c}$ ,  $K_{V_{\text{SH}}}$ ,  $K_{V_{\text{SV}}}$ , and  $K_\eta$  denote corresponding Fréchet derivatives. The key numerical component of our inversion, the global seismic wave propagation solver SPECFEM3D\_GLOBE, is a forward modeling tool that uses a spectral-element method (SEM) to simulate global- or continental-scale wave propagation in fully 3-D Earth models with high precision [Komatitsch and Tromp, 2002a, 2002b]. The East Asia simulation domain includes China, N. Korea, S. Korea, Japan, and Mongolia, as well as parts of Southeast Asia, Burma, Laos, Thailand, Vietnam, Indonesia, Malaysia, and the Philippines. The SEM mesh also incorporates topography (a 4 min global relief model created by subsampling and smoothing ETOPO-2 [National Geophysical Data Center, 2006]) and undulations of the Moho [Basson *et al.*, 2000] and the 410 km and 650 km discontinuities [Kustowski *et al.*, 2008a]. In our inversion, the model is parameterized on the SEM Gauss-Lobatto-Legendre integration points, which have an 8 km lateral spacing and a vertical spacing of less than 5 km in the crust, and a 16 km lateral spacing and an average vertical spacing of ~10 km in the upper mantle.

We start with an initial model which combines 3-D global radially anisotropic mantle model S362ANI [Kustowski *et al.*, 2008a] with 3-D crustal model Crust2.0 [Basson *et al.*, 2000]. The initial source representation is given by the centroid moment tensor (CMT) solution [Ekström *et al.*, 2005]. CMT solutions generally describe earthquake sources very well, but they do have uncertainties due to unmodeled 3-D structure [Hjörleifsdóttir and Ekström, 2010], in particular, with regard to depth. As the first step of this tomographic study, source parameters are reinverted within the initial model using the CMT3D inversion method developed by Liu *et al.* [2004]. In order to obtain good azimuthal coverage, we use seismic waveforms from five high-quality global and regional seismic networks (IU, IL, G, GE, and IC). Source inversions for each earthquake require nine simulations to obtain Fréchet derivatives for nine source parameters. Data and synthetics are bandpass filtered in three complementary period bands, namely, from 30 s to 60 s, 50 s to 100 s, and 80 s to 150 s. Body wave misfits in the period range 30 s–60 s and body wave and surface wave misfits in 50 s–100 s and 80 s–150 s passbands are used in the source inversions. Figure S1 in the supporting information shows an example of a CMT3D inversion result. For this particular earthquake (event 201003140808A), the optimal source solution is chosen with the highest variance reduction when inverting for nine source parameters with zero trace plus double couple constraints. The inversion yields a source depth 3.6 km shallower than the CMT solution. We apply the same source inversion procedure for all events used in the structural inversion (Figure 2). The CMT3D inversion typically places earthquakes at shallower depths (0 km–5 km shallower) by correcting for 3-D structure, specifically the crust (Figure S2). Full waveform source inversion is computationally expensive for hundreds of events. The total cost is equivalent to the CPU time required for about 15 structural iterations, and thus it is computationally prohibitive to perform source inversions after each structural model update. Past experience has shown that such additional source inversions are unnecessary in the period ranges used in the structural inversion.

After the source inversions, we update the 3-D structure based on finite-frequency kernels with fixed source parameters. Synthetic seismograms for the initial 3-D model were calculated for all stations within the model domain (Figure 2). Selecting measurement windows is accomplished based on FLEXWIN [Maggi *et al.*, 2009], an algorithm to automatically pick measurement windows in vertical, radial, and tangential component seismograms. We preprocess both data and synthetics identically by removing any linear trend, tapering, and bandpass filtering. Data records dominated by noise are rejected. FLEXWIN first automatically detects time windows in synthetic seismograms in which waveforms contain distinct arrivals. This automatic phase detection process is motivated by the idea that strong phase arrivals are characterized by a relatively large short-term average/long-term average ratio, which is derived from the envelope of the synthetic seismogram. FLEXWIN decides which windows to keep based on an adequate correspondence between observed and simulated waveforms within these windows. The key window selection criteria are the water level of the short-term average/long-term average ratio for phase detection and acceptance levels for the cross-correlation coefficient, time lag, and amplitude ratio of windowed data and synthetic waveforms. Acceptance levels for the time lag are set to be smaller than half of the minimum period of each passbands, which is one of the criteria that guards against cycle skipping. The windows are fixed for the first six iterations, and subsequently new windows are added after each iteration, as the model improves. Measurement windows are selected in three passbands (Figure 3). The three passbands are 15 s–40 s (short-period passband), 30 s–60 s (intermediate-period passband), and 50 s–100 s (long-period passband) for the first 12 iterations. In subsequent iterations we lowered the lower bounds of the passbands to 12 s, 20 s, and 40 s, respectively.

After selecting measurement windows, frequency-dependent misfits are measured within the chosen windows. The overall traveltime misfit,  $\chi$ , has equal contributions,  $\chi_c$ , from nine categories, namely, measurements from three passbands on three components (Figure 4). Thus, we may write

$$\chi = \frac{1}{N_c} \sum_c \chi_c, \text{ with} \quad (2)$$

$$\chi_c = \sum_{pc} \int \frac{1}{N_{pc}} \left( \frac{\Delta T_{pc}(\omega)}{\sigma_{pc}(\omega)} \right)^2 d\omega \quad (3)$$

where

- $\chi$  misfit function from all  $N_c$  categories;
- $\chi_c$  misfit contribution from category  $c$ ;

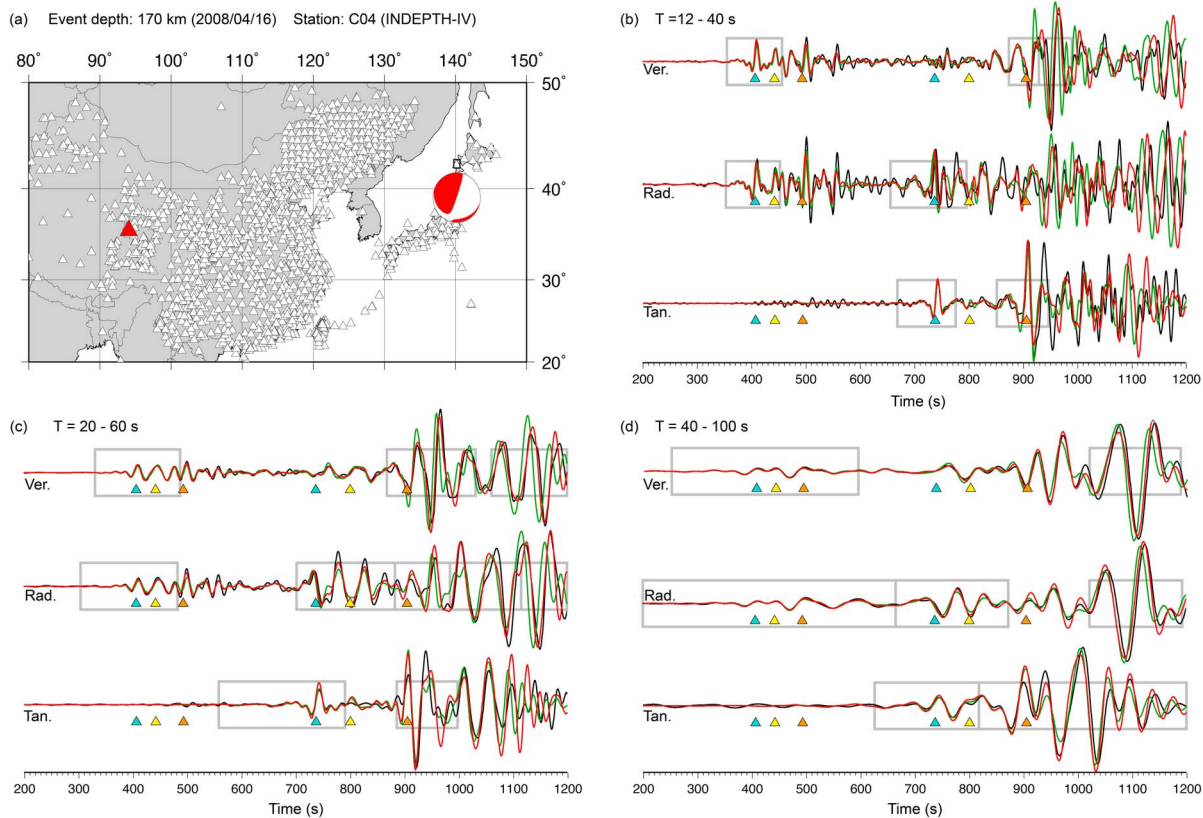


**Figure 3.** Examples of waveforms and misfit measurement windows (grey boxes) used in this study. (a) Map showing the earthquake (red beach ball) and the station (red triangle). Data (black lines), initial model synthetics (green lines), and EARA2014 synthetics (red lines) are filtered in three passbands: (b)  $T = 12 - 40$  s, (c)  $T = 20 - 60$  s, and (d)  $T = 40 - 100$  s. Green triangles mark the predicted direct  $P$  or  $S$  arrivals by IASPEI91, yellow triangles the depth phases  $pP$  and  $sS$ , and orange triangles  $PP$  and  $SS$  arrivals. Compared to the initial model synthetics, EARA2014 synthetics have improved waveform fits.

$N_c$	number of categories ( $N_c = 9$ );
$N_{pc}$	number of measurements in category $c$ ;
$\Delta T_{pc}(\omega)$	traveltime misfit at frequency $\omega$ for measurement $p$ in category $c$ ;
$\sigma_{pc}(\omega)$	uncertainty of traveltime misfit measurement.

Adjoint sources are constructed using traveltime misfit measurements for all picked phases, e.g., body wave phases (direct  $P$  and  $S$ ,  $pP$ ,  $sP$ ,  $sS$ ,  $pS$ ,  $PP$ , and  $SS$ ) and surface waves (Rayleigh and Love). We use both body wave and surface wave misfits in the intermediate- and long-period passbands but only body wave misfits in the short-period passband, because CRUST2.0 cannot be used to simulate short-period surface waves. The adjoint sources assimilate the misfit as simultaneous fictitious sources, and the interaction of the resulting adjoint wavefield with the regular forward wavefield forms the event kernels. All event kernels are summed to obtain the gradient or Fréchet derivative, which is preconditioned and smoothed to obtain the final model update. The diagonal of the Hessian matrix is chosen as a preconditioner [Luo et al., 2013], and the preconditioned kernels are smoothed by a Gaussian with a width of 5 km in the vertical plane and 100 km in the horizontal plane for the first five iterations and 60 km afterward. The optimal step length for the conjugate gradient model update is chosen based on a line search (Figure 4a). In order to reduce the computational cost we chose a subset of 20 events (Figure 2) to perform the line search (Figure 4a) in a set of six to ten candidate models. The updated model is used as the starting model for the next iteration for further structural refinement. The same procedure is repeated until no significant reduction in misfit is observed, in our case, after 20 iterations (Figure 4b). The new radially anisotropic model of East Asia is named EARA2014 (**E**ast **A**sia **R**adially **A**nisotropic **M**odel 2014). The production of EARA2014 consumed about 8 million CPU hours on supercomputers hosted by the Texas Advanced Computing Center.

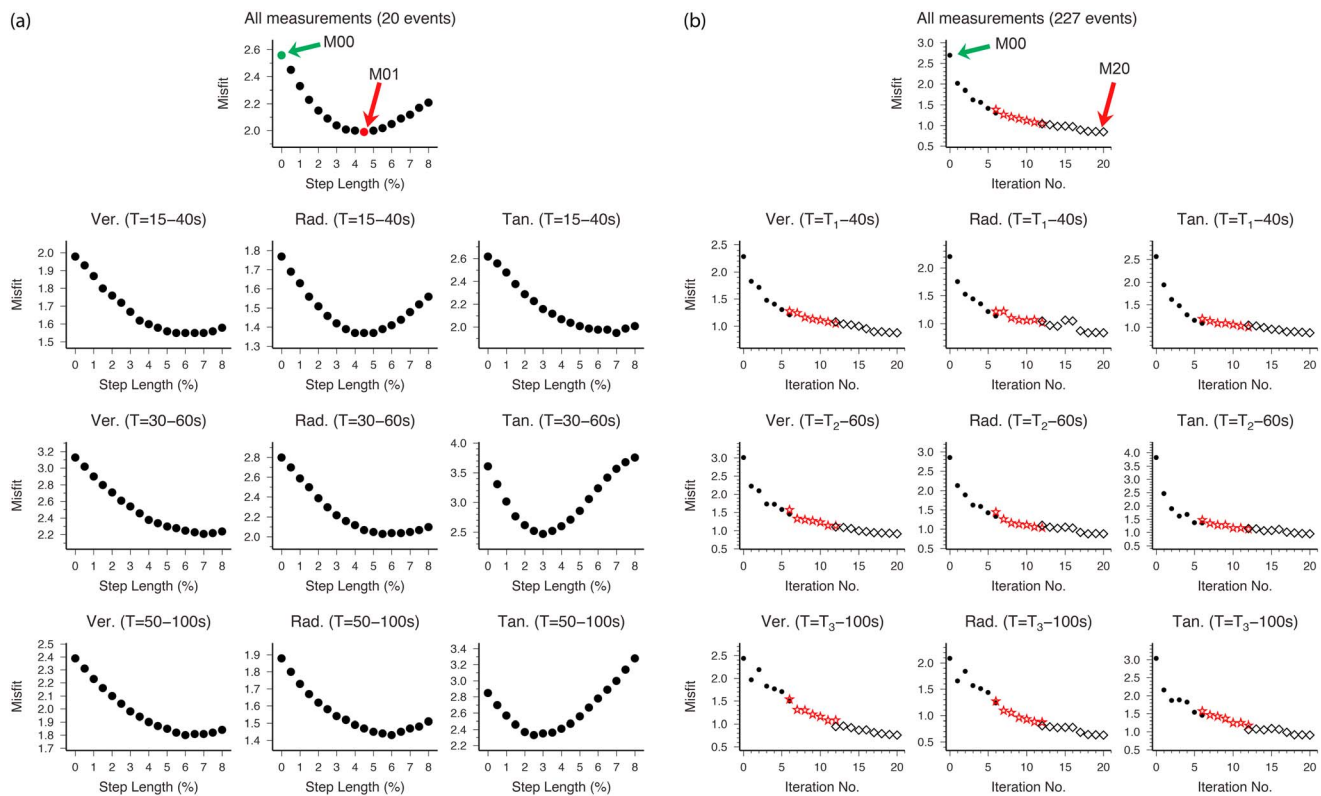


**Figure 4.** Iteration steps illustrated with (a) a line search example using traveltime misfits from a sub-dataset of 20 events (red beach balls in Figure 2), and (b) traveltime misfit evolution of the entire data set (227 events). For the initial model (M00) line search, the first model update (M01) is chosen at a step length of 4.5%, where a traveltime misfit minimum is located (Figure 4a). The overall traveltime misfits decrease when the tomographic inversion proceeds (Figure 4b). For the first five iterations, misfits are measured for the same set of measurement windows (black dots), from the sixth to the eleventh iterations, measurement windows are updated with FLEXTWIN at each iteration (red stars), and from the twelfth to the twentieth iterations the cross-correlation coefficient for window selection is lowered from 0.8 to 0.75 (black diamonds).  $T_1$ ,  $T_2$ , and  $T_3$  (the lower bounds of the period passbands) are 15 s, 30 s, and 50 s, respectively, for the first 12 iterations. They are lowered to 12 s, 20 s, and 40 s, respectively, in subsequent iterations.

### 3. Model Quality Assessment

Before diving into the interpretation of features observed in the new seismic images, we need to assess the quality of model EARA2014. This will ensure that later interpretations are well founded on faithful mapping of information contained in seismic waveforms to elastic properties of the Earth's interior. Our model quality assessment focuses on two aspects, namely, methodology and data coverage. We assess model quality by examining waveform misfit reduction, establishing regions with reasonably good data coverage, comparisons with previous tomographic models, performing resolution tests at several locations of interest, and an inversion with a different initial model.

#### 3.1. Waveform Fitting

Compared to the initial model, final model EARA2014 predicts 3-D wave propagation much better, as illustrated in Figure 3. Adjoint tomography takes three-component body waves in all three frequency bands, and surface waves in the intermediate- and long-period passbands as inputs. Figures 3b–3d show examples of waveforms recorded by a station in Tibet from an intermediate-depth earthquake (170 km depth, Figure 3a). Although the inversion only assimilates measurements in selected windows (grey boxes in Figures 3b–3d), the waveform fit (both phase and amplitude) improves not only in these windows but also in segments of the seismograms that were not selected initially. These improvements are most prominent for wave trains arriving much later than the main body wave phases. In the short-period passband (12 s–40 s), later arriving phases contain short-period surface waves and multireflected body waves, showing good fits between EARA2014 synthetics and the data (Figure 3b), especially considering the complex crustal structure these waves have propagated through. With increasing iterations, traveltime misfits and their standard deviations are significantly reduced

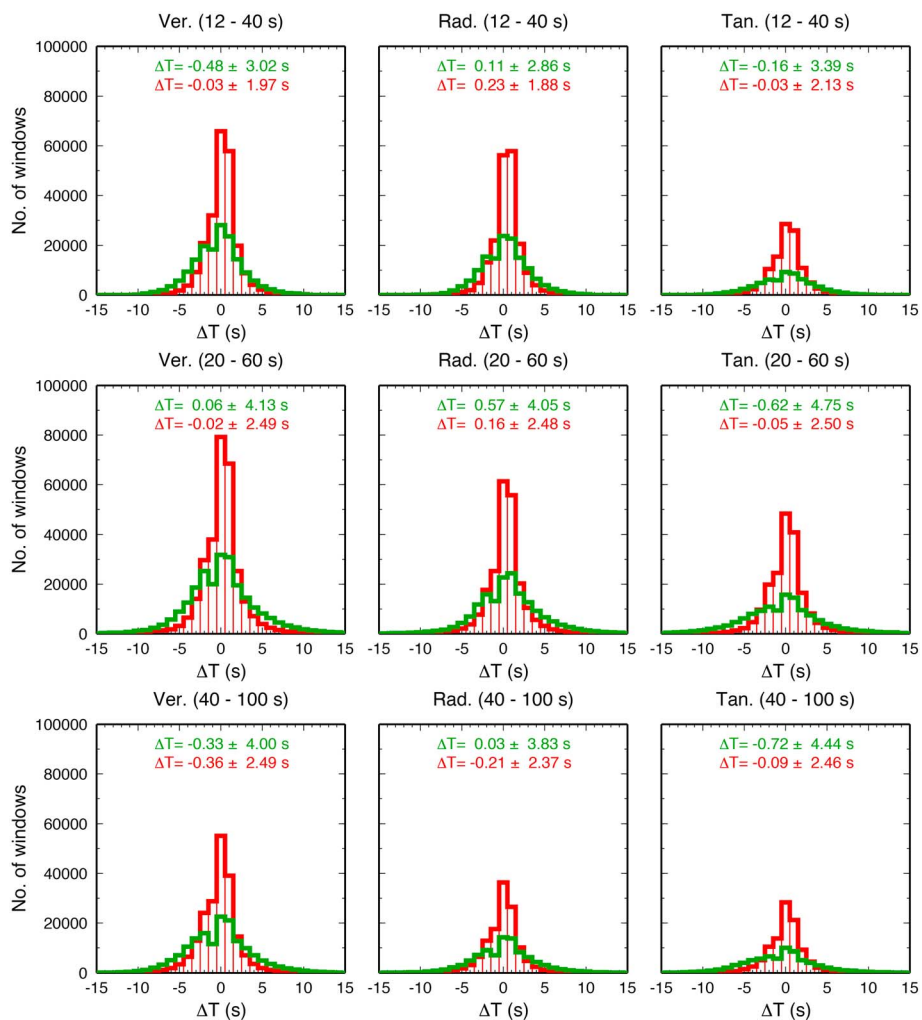


**Figure 5.** Travelttime anomaly histograms based on cross correlations between data and the initial model synthetics (green), and data and the final model (EARA2014) synthetics (red), showing the overall improvement in waveform fits from the initial model to EARA2014. There are a total of 1,243,187 measurements in all categories for the initial model, and a total of 1,694,498 measurements for EARA2014.

(Figures 4b and 5). Travelttime misfit decreases smoothly and consistently (Figure 4b). Amplitude anomalies are not included in the inversion, and thus the amplitude misfit reduction (Figure S3) is more ragged and strongly sensitive to increasing waveform complexity when introducing shorter period waves or waveforms with less similarity to the data (e.g., when the selection criterion for cross-correlation coefficients is lowered from 0.8 to 0.75).

Statistically, using the same selection criteria, the number of measurement windows went up from an initial  $\sim 1.2$  million to the final  $\sim 1.7$  million (Figure 5), and the mean and standard deviation of the travelttime misfits changed from the initial  $-0.12 \pm 3.88$  s to the final  $-0.03 \pm 2.32$  s, with a significant reduction in standard deviation by 1.56 s. Because seismic attenuation is not inverted for at this stage, a slight improvement in amplitude fits can be attributed to wave focusing and defocusing due to 3-D elastic heterogeneity, for example, the amplitude anomaly standard deviation of 40 s–100 s waves on tangential components decreased from 0.28 to 0.25 (Figure S4). Further improvement in amplitude misfit reduction requires parameterization of 3-D seismic attenuation by minimizing both travelttime and amplitude misfits [Zhu et al., 2013].

Analyzing data from 39 earthquakes that were not used in the inversion further assesses EARA2014's ability to predict seismic waveforms in East Asia. The number of measurement windows went up from an initial 105,187 to the final 148,574 (Figure S5), and the mean and the standard deviation went from the initial  $-0.10 \pm 4.24$  s to the final  $-0.24 \pm 3.11$  s, with a reduction in standard deviation by 1.13 s. Again, the amplitude fits improve only slightly for reasons stated above (Figure S6).

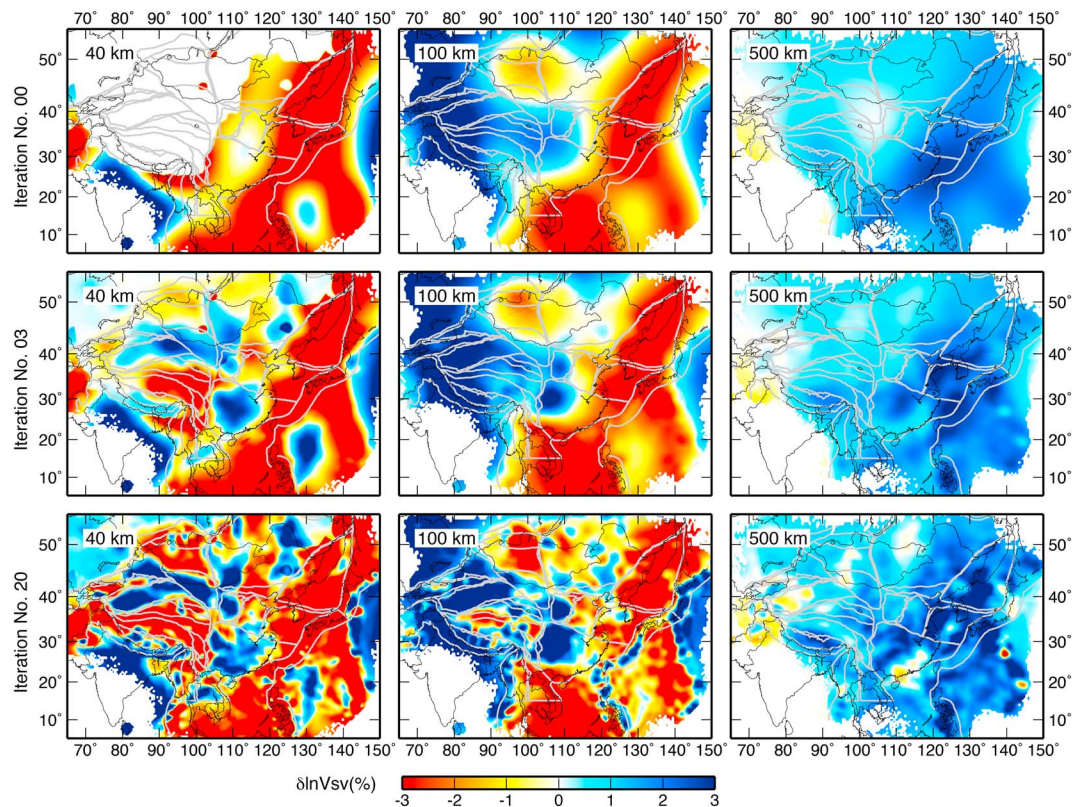


**Figure 6.** Constant depth map views of the initial model (S362ANI + Crust2.0) (top row), the third iteration model (middle row), and the twentieth iteration model (EARA2014) (bottom row) at depths of 40 km (left column), 100 km (middle column) and 500 km (right column). Tomographic images sharpen and more detailed seismic structures are revealed with increasing iterations.  $V_{\text{Sy}}$  anomalies are relative to 3-D crustal model (Crust2.0) in the crust and relative to global 1-D model STW105 [Kustowski et al., 2008a] in the mantle. The regional mean of wave speed anomalies is not removed.

### 3.2. Approximate Hessian–Proxy for Data Coverage

The diagonal Hessian matrix is chosen as the preconditioner  $\mathbf{P}$  [Luo et al., 2013]:

$$\begin{aligned} \mathbf{P} &= \lim_{\mathbf{x}' \rightarrow \mathbf{x}} \sum_s \iint \partial_t^2 \mathbf{s}^\dagger(\mathbf{x}, -t) \cdot \mathbf{G}(\mathbf{x}, \mathbf{x}', t - t') \cdot \partial_t^2 \mathbf{s}(\mathbf{x}', t') dt dt' \\ &\approx \sum_s \int \partial_t^2 \mathbf{s}^\dagger(\mathbf{x}, -t) \cdot \partial_t^2 \mathbf{s}(\mathbf{x}, t) dt, \end{aligned} \quad (4)$$

where the following approximation is used:

$$\lim_{\mathbf{x}' \rightarrow \mathbf{x}} \mathbf{G}(\mathbf{x}, \mathbf{x}', t - t') \approx \mathbf{I} \delta(t - t'). \quad (5)$$

The preconditioner takes into account amplitude effects due to geometrical spreading of both the forward and adjoint wavefields (equation (4)). Therefore, it also serves as a good proxy for data coverage, indicating model regions that are well resolved given the data coverage.

We chose preconditioner values over a certain threshold to highlight regions with reasonably good data coverage at each depth. Figure S7 shows that, with increasing depth, the resolvable area shrinks. In the crustal and uppermost mantle depth range (20 km–250 km), the resolvable region includes China, southernmost Russia, Mongolia, Kazakhstan, N. Korea, S. Korea, Japan, Burma, Laos, Thailand, Vietnam, Cambodia, Malaysia, the Philippines, the Philippine Sea, the Japan Sea, the East China Sea, and the South China Sea. Between depths of 250 km and 600 km, data coverage diminishes in southernmost East Asia, e.g., in Malaysia, Cambodia, and southern Vietnam. Between 600 km and 900 km, resolution is further lost in southernmost Russia, Kazakhstan, the southwestern part of the South China Sea, Thailand, Burma, and the eastern part of the Philippine Sea. In maps showing EARA2014 model parameters, unresolved regions are masked out for preconditioner values below the threshold.

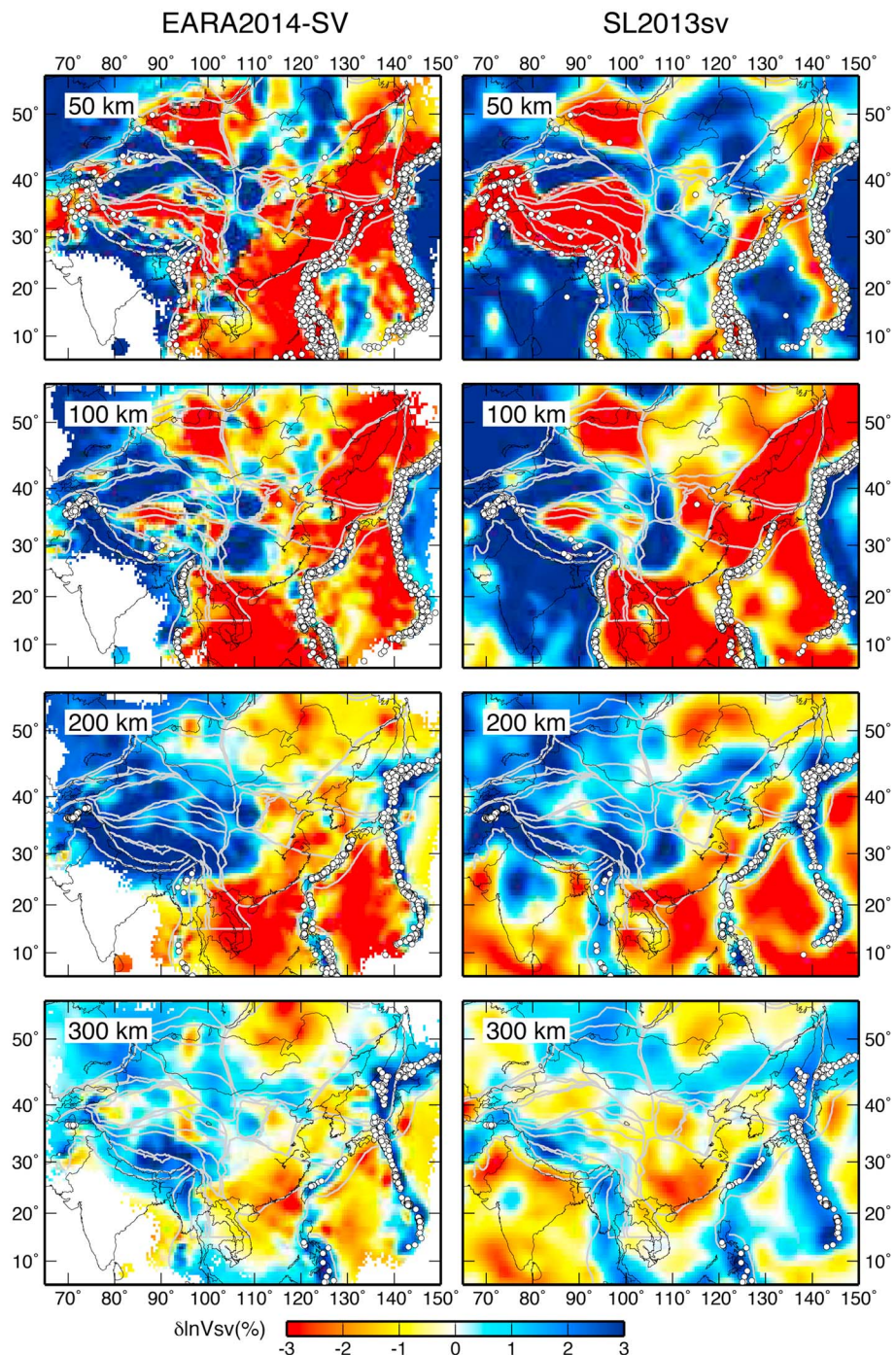


**Figure 7.** Comparison between (left column) EARA2014-SV and (right column) SL2013sv [Schaeffer and Lebedev, 2013] at various depths. Both models are shown after the regional mean has been removed. White dots indicate earthquakes that occurred within a 5 km (at a depth of 50 km), 25 km (at a depth of 100 km), or 50 km (at depths of 200 km and greater) distance of each depth slice. Note that  $V_{sv}$  anomalies of both models are relative to 3-D crustal model (Crust2.0) at depths shallower than the Moho.

### 3.3. Model Comparison

In this section we visually inspect qualitative correlations of surface expressions with high-V and low-V anomalies in EARA2014 and discuss similarities and differences between EARA2014 and previous tomographic models.

EARA2014 is a refined version of the initial model, which combines a smooth global mantle model, S362ANI [Kustowski et al., 2008a], with crustal model Crust2.0. Figure 6 shows that the updated images gradually

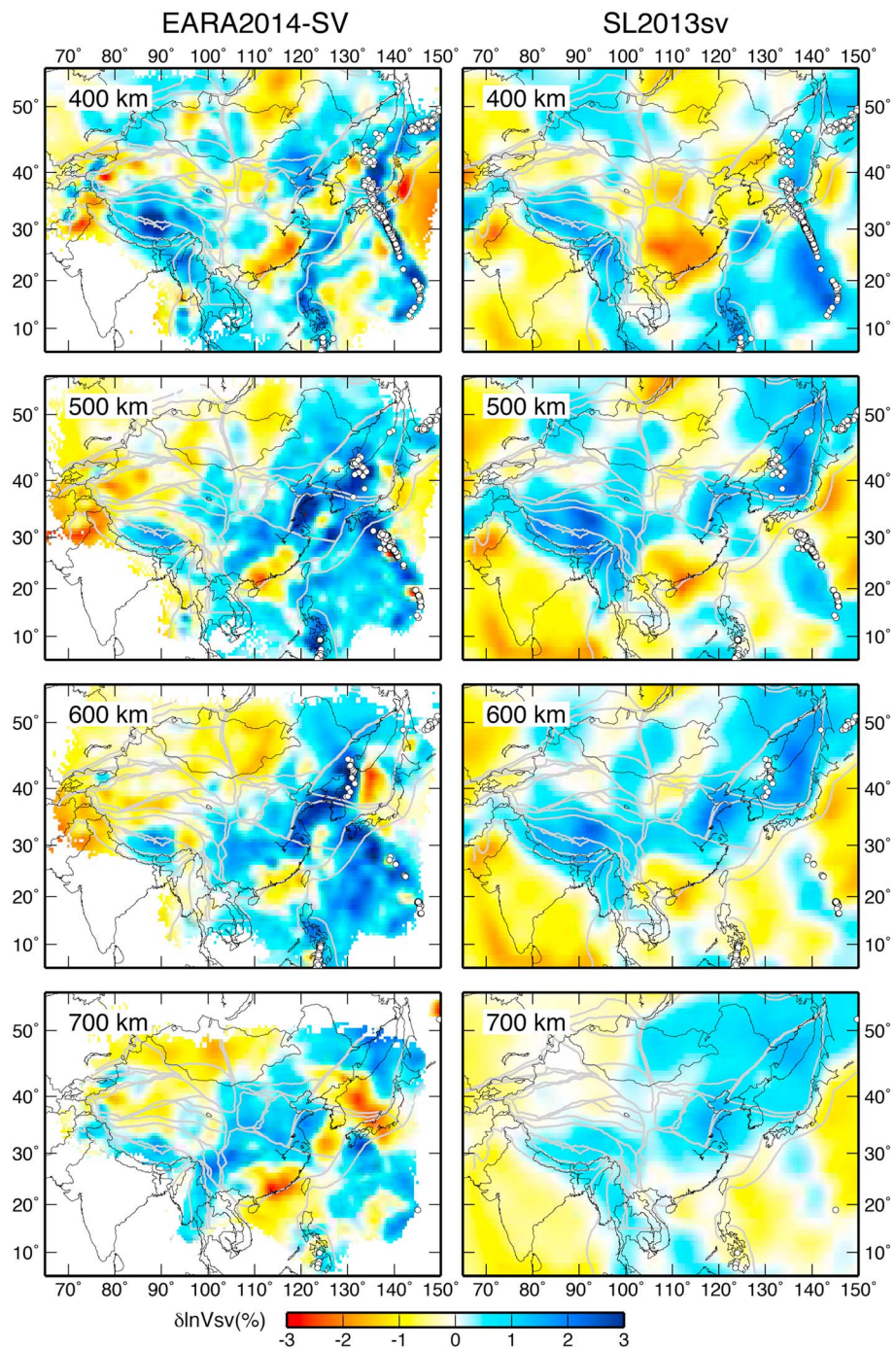
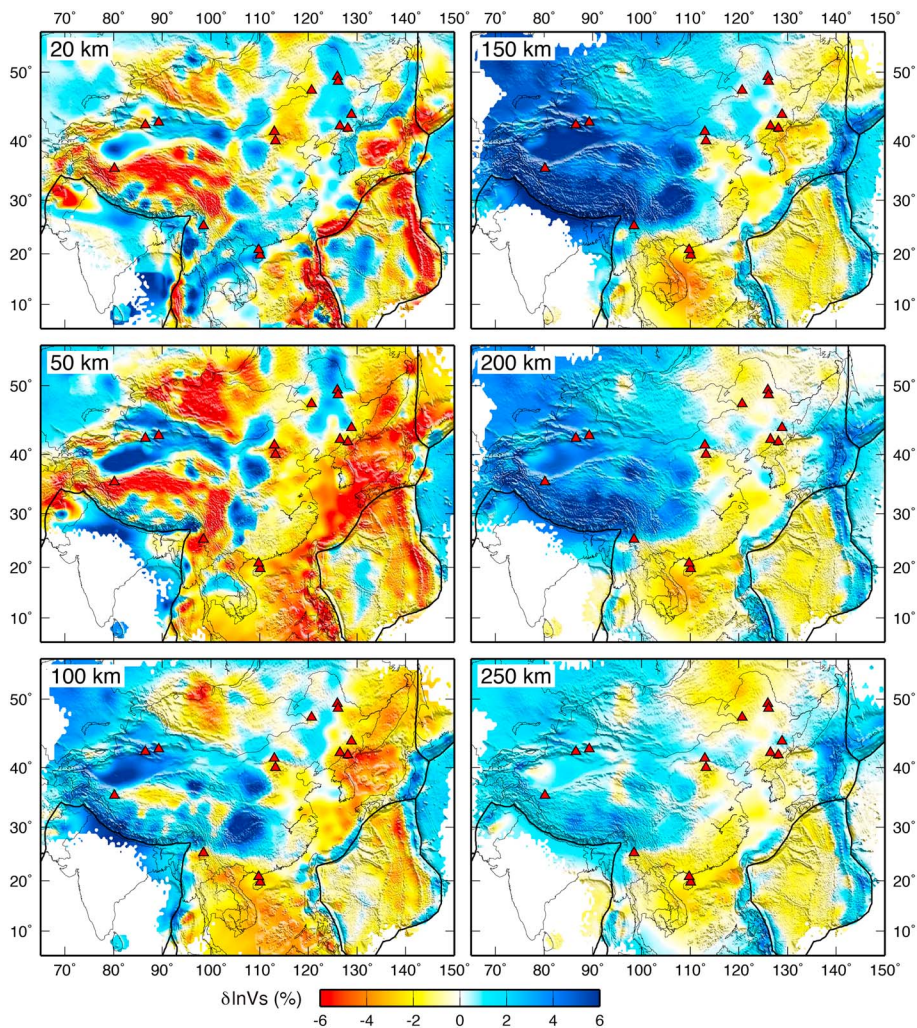


Figure 7. (continued)

reveal clear small-scale features correlating with known tectonic units at depths of 40 km and 100 km and delineating slab relics beneath Southeast Asia at 500 km depth. High-V anomalies at a depth of 40 km (Figure 6) correlate very well with the Himalaya Block and the Junggar, Sichuan, Dongting, Tarim, Nanshan, East Gobi, Erlian, Songliao, and West Philippine Basins (Figure 1). High-V anomalies inside the mantle (at a depth of 100 km) strongly correlate with stable tectonic units, such as the Tarim and Junggar Basins, the Ordos Block, and the Yangtze Platform. Low-V anomalies at a depth of 40 km coincide with the Qiangtang Block, the Songpan Ganzi Fold Belt, the Qilian Fold, the Chuandian Block, and the Great Xing'an Range. Low-V anomalies also are highly localized within the Altay-Sayan Mountain Range in the crust (a depth of 40 km) and



**Figure 8.** Voigt-Reuss-Hill average shear wave speed maps of EARA2014 at constant depths, in percent from Crust2.0 in the crust and from 1-D model STW105 in the mantle, superimposed on topography. The constant depth is shown in the top left of each map. Red and blue colors denote low and high wave speeds respectively. Red triangles mark active volcanoes. The regional mean of wave speed anomalies is not removed.

mantle (a depth of 100 km). Sharp wave speed contrasts across tectonic unit boundaries and strong correlations of wave speed anomalies with surface expressions provide further evidence of a much higher image resolution in EARA2014 compared to the initial model.

Figure 7 shows that EARA2014-SV resembles the latest high-resolution global shear wave model SL2013sv [Schaeffer and Lebedev, 2013] in East Asia, which uses seismic waveforms with the shortest period of 11 s. In regions where SL2013sv has equally good data coverage, EARA2014-SV and SL2013sv have very similar wave speed anomaly patterns and strengths. For example, both models image very strong and localized low-V anomalies beneath the Tibetan Plateau and the Altay-Sayan Mountain Range in the crust and uppermost mantle (at depths of 50 km and 100 km). Both models also reveal a broad high-V structure beneath central and southern Tibet at 400 km depth, extending to the bottom of the mantle transition zone. However, as our study has much denser data coverage in East China, EARA2014 captures much stronger and more continuous high-V narrow slabs along the northwestern Pacific margin (at depths between 200 km and 400 km), which match the subduction zone distribution of seismicity.

Compared to previous regional shear wave speed models inverted from shear waves and/or surface waves [Priestley et al., 2006; Obrebski et al., 2012; Yang et al., 2012; Zhao et al., 2012], EARA2014 (Figure 8) has much sharper image resolution due to its superior data coverage and more solid theoretical foundation. Compared

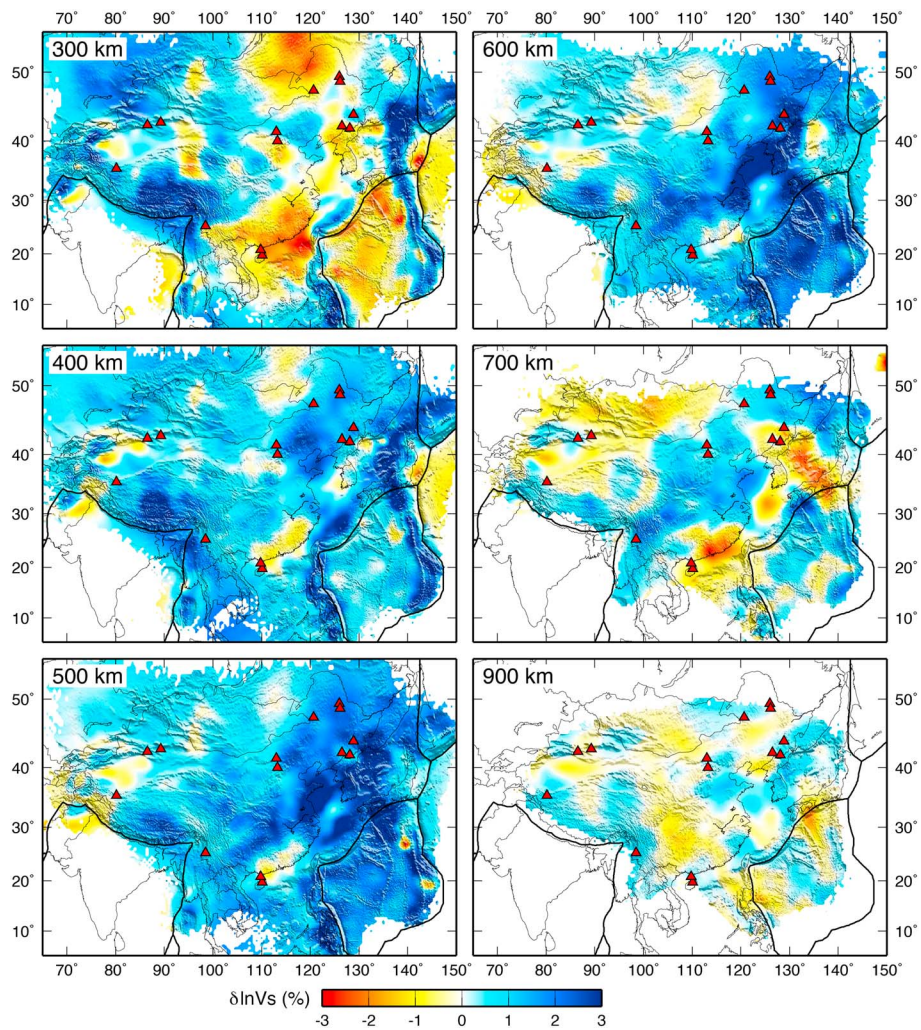
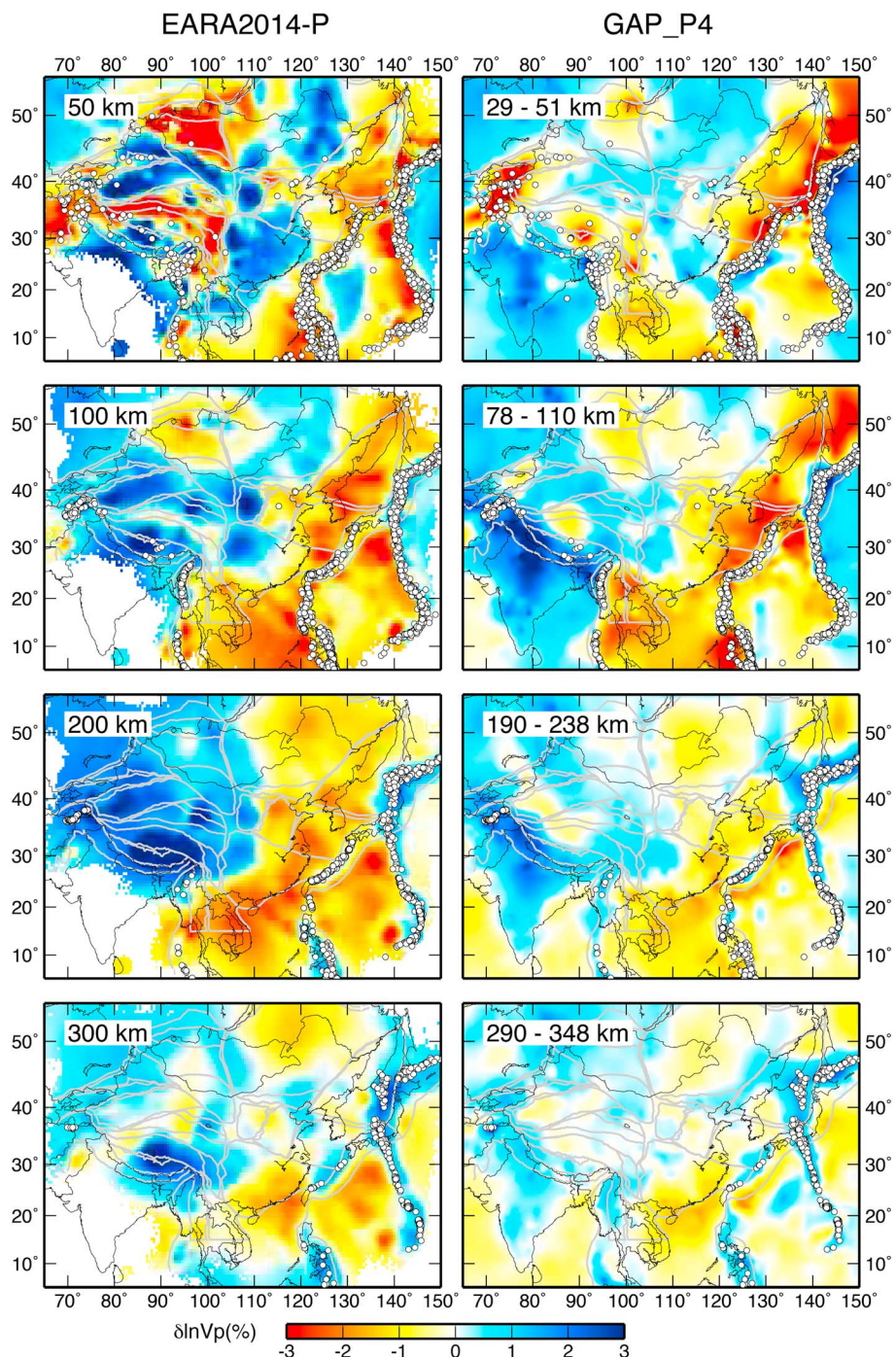


Figure 8. (continued)

to the  $V_{SV}$  model by Priestley *et al.* [2006] (see their paper, Figure 4), EARA2014 (Figure 8) shows well-defined high-V and low-V anomaly patterns beneath continental East Asia and captures well-confined narrow high-V slab features. Figure S8 provides a comparison of EARA2014 with another regional tomography model, CH11sv, inverted based on shear and surface waves by Obrebski *et al.* [2012]. Robust features, such as the Yangtze Platform, the Ordos Block, and a fragmented slab inside the mantle transition zone, show up as high-V anomalies in both models. However, high-V anomalies in EARA2014 are much stronger and more sharply confined within tectonic unit boundaries than in CH11sv. High-V anomalies beneath the Pamir and Tianshan Mountain Ranges are overestimated in CH11sv and have no correlation with surface expressions (depths of 40 km and 100 km in Figure S8). On the contrary, high-V anomalies in EARA2014 beneath the Tarim, Junggar, and Nanshan Basins are very well correlated with surface tectonics. Wave speed anomalies of EARA2014 beneath the Tibetan Plateau are also consistent with high-resolution short-period (10 s–60 s) surface wave tomography by Yang *et al.* [2012] (Yang2012sv, Figure S9). Both models have strong and well-confined low-V anomalies beneath the Tibetan Plateau. Despite numerous similarities between EARA2014 and Yang2012sv in western China, significant differences exist even for long-wavelength structures. For example, at a depth of 30 km, in the image of Yang2012sv low-V anomalies are ubiquitous beneath the Tibetan Plateau; however, in the image of EARA2014 low-V anomalies are more confined beneath the Songpan Ganzi Fold Belt and the northern Qiangtang Block (Figure S9).

Compared to the high-resolution shear wave tomographic images obtained by Zhao *et al.* [2012] (see their paper, Figure 4), EARA2014 (Figure 8) reveals consistent long-wavelength structures, yet presents stronger



**Figure 9.** Comparison between (left column) EARA2014-P and (right column) GAP\_P4 [Obayashi et al., 2013] at various depths. Both models are shown after removal of the regional mean wave speed anomalies. Note that  $V_p$  anomalies of EARA2014 are relative to 3-D crustal model (Crust2.0) at depths shallower than the Moho. Depth slices of GAP\_P4 are given in certain depth ranges because of the model block size used in their inversion. White dots indicate earthquakes that occurred within a 5 km (at a depth of 50 km), 25 km (at a depth of 100 km), or 50 km (at depths of 200 km and greater) distance of each depth slice.

wave speed anomalies in more homogenized long-wavelength structures. Such discrepancies could be due to the different data sets used in the two studies. EARA2014 is obtained based on both body waves (12 s–100 s) and surface waves (20 s–100 s), while the Zhao et al. [2012] SV model is solely constrained with direct shear waves in the period range from 10 s to 50 s. The discrepancies could also be due to the different measurements

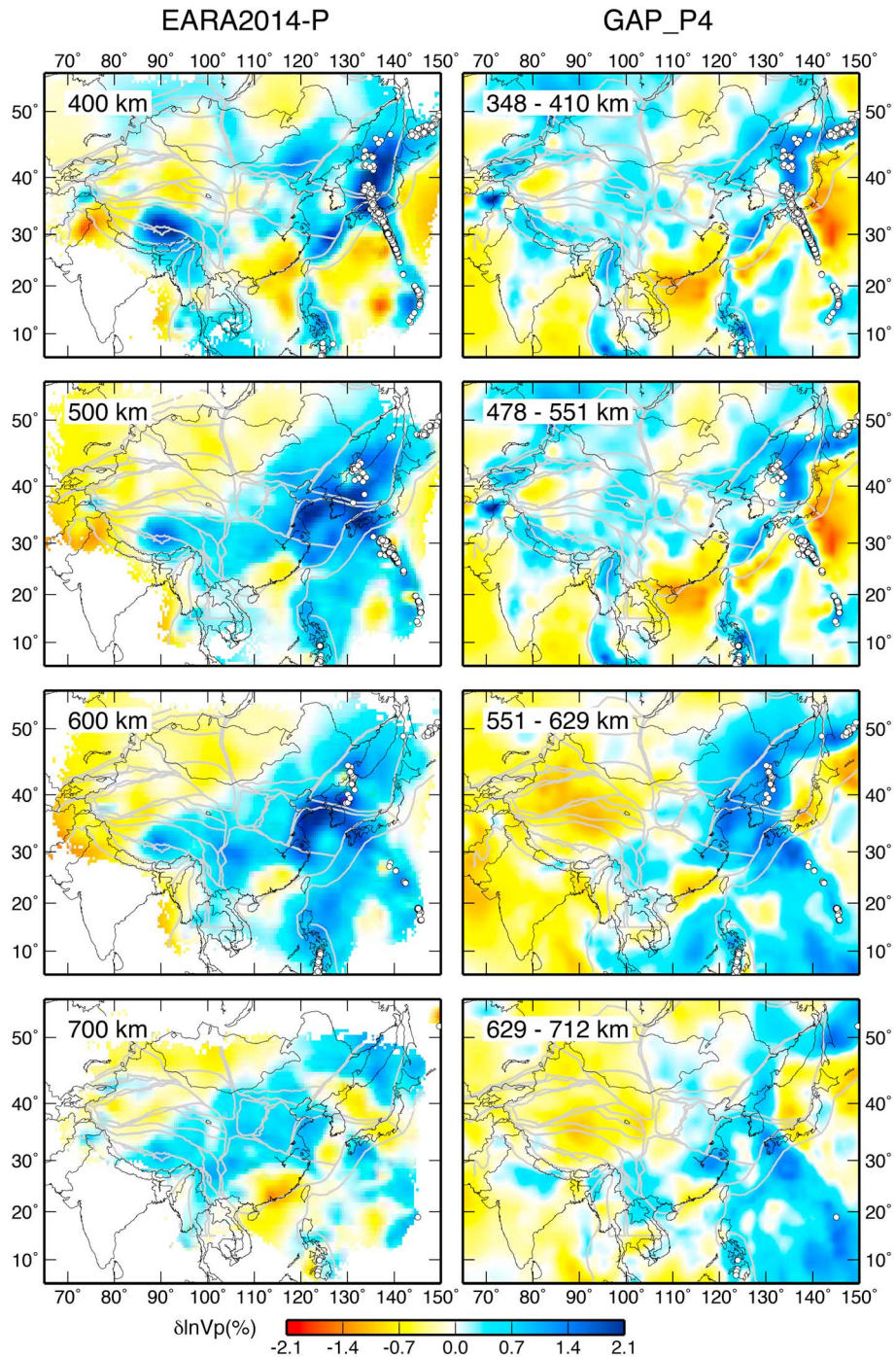
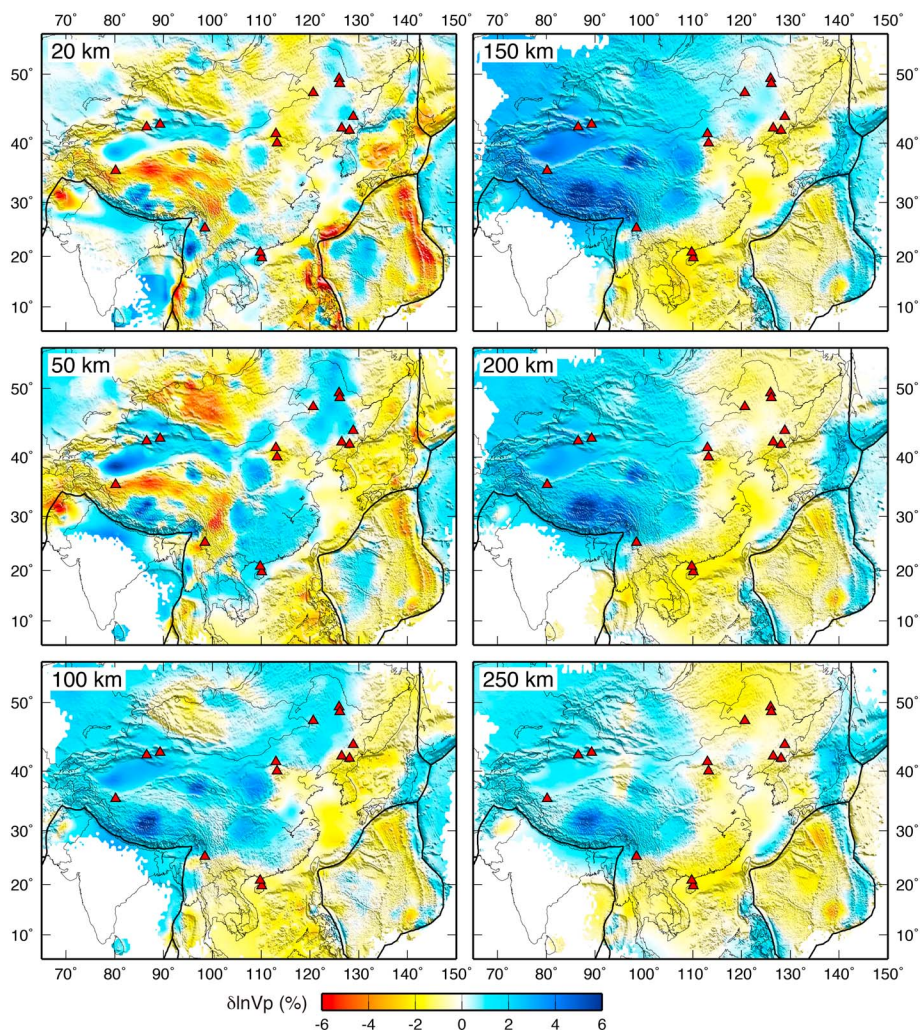


Figure 9. (continued)

used in the inversions. Instead of absolute traveltime misfit measurements (used in our study), their inversion uses differential traveltime measurements between stations as input. Consequently, their model emphasizes local short-wavelength variations rather than long-wavelength structures.

Figure 9 shows a comparison between EARA2014-P (Figure 10) and a previous compressional wave speed model, GAP\_P4 [Obayashi *et al.*, 2013]. GAP\_P4 is inverted based on ray theoretical kernels using a large number of *P* wave arrival times, *PP*-*P* differential travel times, and relative *P* wave travel times between two stations. Similar to GAP\_P4, EARA2014-P captures a well-defined oceanic slab morphology in the upper mantle down to the mantle



**Figure 10.** Voigt-Reuss-Hill average compressional wave speed maps of EARA2014 at constant depths (in percent from Crust2.0 in the crust and from 1-D model STW105 in the mantle). The regional mean of wave speed anomalies is not removed.

transition zone, high-V anomalies beneath the stable tectonic units of the Ordos block and the Yangtze Platform, a stagnant high-V slab beneath East China inside the mantle transition zone, and low-V anomalies beneath the back-arc basins and marginal seas of Japan and China. However, EARA2014-P differs from GAP\_P4 in terms of wave speed anomaly patterns and amplitudes. EARA2014-P has the following major distinct features (Figures 9 and 10): (1) A strong broad high-V ( $\delta \ln V_p > 1.5\%$ ) structure exists beneath the Tibetan Plateau below 100 km and extends to the bottom of the mantle transition zone. (2) Strong high-V anomalies exist beneath the Tarim, Nanshan, Junggar, Sichuan, and Ordos Basins down to about 250 km. (3) Pronounced low-V anomalies ( $\delta \ln V_p < -3\%$ ) appear beneath the Qiangtang Block, the Songpan Ganzi Fold Belt, the Qilian Fold, the Chuandian Block, and the Altay-Sayan Mountain Range in the middle to lower crust. (4) Strong high-V anomalies indicate slab relics inside the mantle transition zone. (5) T-shaped low-V anomalies appear in the lower mantle at a depth of 700 km beneath the Japan Sea and the East China Sea, indicating possible lower mantle upwellings.

Compared to previous compressional wave speed models [Huang and Zhao, 2006; Li and van der Hilst, 2010; Wei *et al.*, 2012; Obayashi *et al.*, 2013], EARA2014-P (Figure 10) not only shows much stronger  $V_p$  anomalies and better correlations with surface tectonics in the uppermost 100 km but also captures slab morphology better, with stronger high-V in the depth range from 100 km to 400 km that matches the seismicity distribution. However, due to the fact that our data set is not as sensitive to bulk sound speed  $V_C$  as to shear wave speeds, slab morphology in the compressional wave speed images (Figures 9 and 10) is not as sharply defined as in the shear wave speed images (Figures 7 and 8).

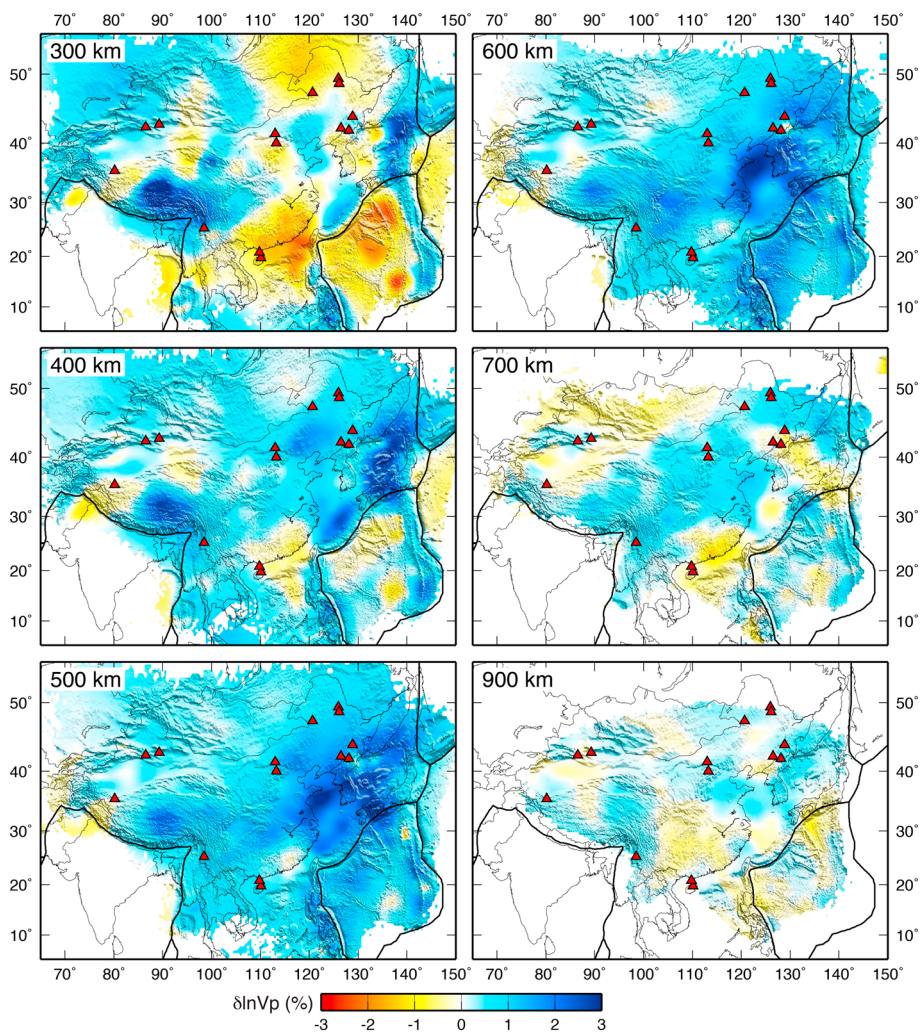
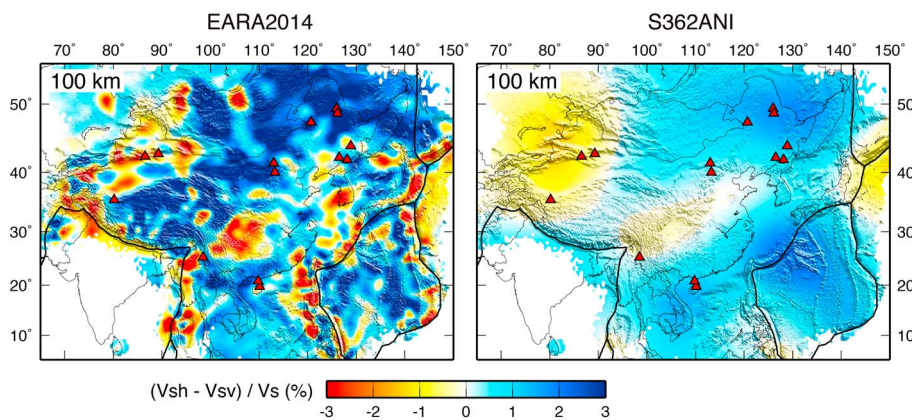


Figure 10. (continued)

Visual comparison of radial anisotropy between EARA2014 and S362ANI [Kustowski *et al.*, 2008a] (Figure 11) demonstrates that EARA2014 retains the long-wavelength pattern of S362ANI (the initial model). However, at 100 km depth, EARA2014 shows very distinct short-wavelength variations of radial anisotropy in terms of both pattern and amplitude: (1) widespread strongly positive radial anisotropy ( $\zeta > 3\%$ ) below Tibet, northern China, Mongolia, and the Philippine Sea Plate; (2) localized strongly negative radial anisotropy ( $\zeta < -3\%$ ) below the Yangtze Platform, the Altay-Sayan Mountain Range, the southern tip of Lake Baikal, parts of the marginal seas (South China Sea, East China Sea, and Japan Sea), and the major subduction zones, such as Japan and Ryukyu.

The widespread strongly positive radial anisotropy of EARA2014 (Figure 11), in terms of long-wavelength variations, is qualitatively consistent with other global radial anisotropy models, such as savani [Auer *et al.*, 2014], S362WMANI [Kustowski *et al.*, 2008a], SEMUM2 [French *et al.*, 2013], and SEMUCB-WM1 [French and Romanowicz, 2014] but different from SAW642ANb [Panning *et al.*, 2010] underneath Tibet, where SAW642ANb has negative radial anisotropy [see Auer *et al.*, 2014, Figure 11]. However, the strong negative radial anisotropy features in EARA2014 at 100 km depth, which are mostly short-wavelength variations, are not seen in any of the global models. Several regional radial anisotropy studies either confirm or dispute short-wavelength features in EARA2014 [Chen *et al.*, 2009; Lebedev *et al.*, 2009; Agius and Lebedev, 2013]. A surface wave dispersion study by Lebedev *et al.* [2009] shows absence of anisotropy in the lithospheric mantle beneath the Yangtze Platform, where EARA2014 indicates strongly negative anisotropy. Positive radial anisotropy in the uppermost mantle beneath Tibet is found in the study of Agius and Lebedev [2013], and this agrees with EARA2014. Another



**Figure 11.** Comparison of radial anisotropy,  $\xi = (V_{SH} - V_{SV})/V_S$ , between EARA2014 and S362ANI (the initial model) at 100 km depth.  $V_S$  is the Voigt-Reuss-Hill average shear wave speed.

surface wave study by *Chen et al.* [2009] shows certain radial anisotropy patterns similar to EARA2014 at 100 km depth, for example, positive anisotropy beneath the Lhasa Block and strong negative anisotropy beneath Burma, the southern Chuandian Block, and the Sichuan Basin but other patterns different from EARA2014, such as negative anisotropy in the western Qiangtang Block and the eastern Tarim Basin, where EARA2014 displays positive anisotropy.

Different model parameterizations and data coverage can lead to differences in radial anisotropy between our model and previous models. Previous regional studies are mostly based on surface wave analyses, and models are parameterized with radial anisotropy in both the crust and the mantle. Our study limits shear wave radial anisotropy between the Moho and the 650 km discontinuity. EARA2014 radial anisotropy is constrained by not only surface waves but also body waves on three components. However, we cannot rule out that small wavelength anisotropy patterns in EARA2014 may be artificial and can be caused by tradeoff between isotropic heterogeneities and anisotropy [*Bodin et al.*, 2015]. Further tests of the robustness of EARA2014 radial anisotropy are needed to ensure a correct model interpretation. In the next section we investigate some of these tradeoffs based on the point spread function.

### 3.4. Point Spread Function Tests for Locations of Interest

The resolving capability of adjoint tomography is difficult to assess, as routine checkerboard tests are computationally prohibitive and provide limited information [*Lévéque et al.*, 1993; *Fichtner and Trampert*, 2011a, 2011b]. On top of that, because checkerboard tests bear the same theoretical foundation as the adjoint tomographic inversion, the accuracy of the methodology itself is impossible to examine [*Qin et al.*, 2008]. The latest resolution analysis method in full waveform inversion, based on the Fourier-domain approximate Hessian proposed by *Fichtner and Trampert* [2011b], overcomes the limitations of checkerboard tests and provides additional useful information, such as image distortion and resolution length, while being relatively computationally efficient (about six conjugate gradient iterations). However, the implementation of such a method is beyond the scope of this study. Instead, following *Zhu et al.* [2012b], we chose to perform simpler and more straightforward “point spread function” (PSF) tests to evaluate local resolution for a few locations of interest and to probe the degree of image blurring and distortion of the final model. The PSF test evaluates the resolution of a particular point of interest in the model by the degree of “blurring” of a perturbation located at that point and by revealing the tradeoff with other model parameters. We added perturbations represented by 3-D Gaussians at eight locations of interest, with a 120 km radius and a maximum  $\pm 4\%$  perturbation at the center (Figure S10). Although there is a certain degree of smearing, the  $V_{SV}$  PSFs recover the main features of the perturbations while exhibiting negligible tradeoff with  $V_{SH}$  and  $V_C$ , confirming that  $V_{SV}$  wave speed anomalies are well resolved in the following regions: (1) low-V beneath the Altay-Sayan Mountain Range in the upper mantle (Figure S10a); (2) low-V beneath the Changbai and Hainan volcanoes at the bottom of the mantle transition zone (Figures S10b and S10d); (3) high-V beneath the Yangtze Platform inside the mantle transition zone (Figure S10c); (4) low-V beneath the northern Philippine Sea Plate in the upper mantle (Figure S10e); (5) high-V beneath the West Philippine Basin in the uppermost mantle (Figure S10f); (6) high-V

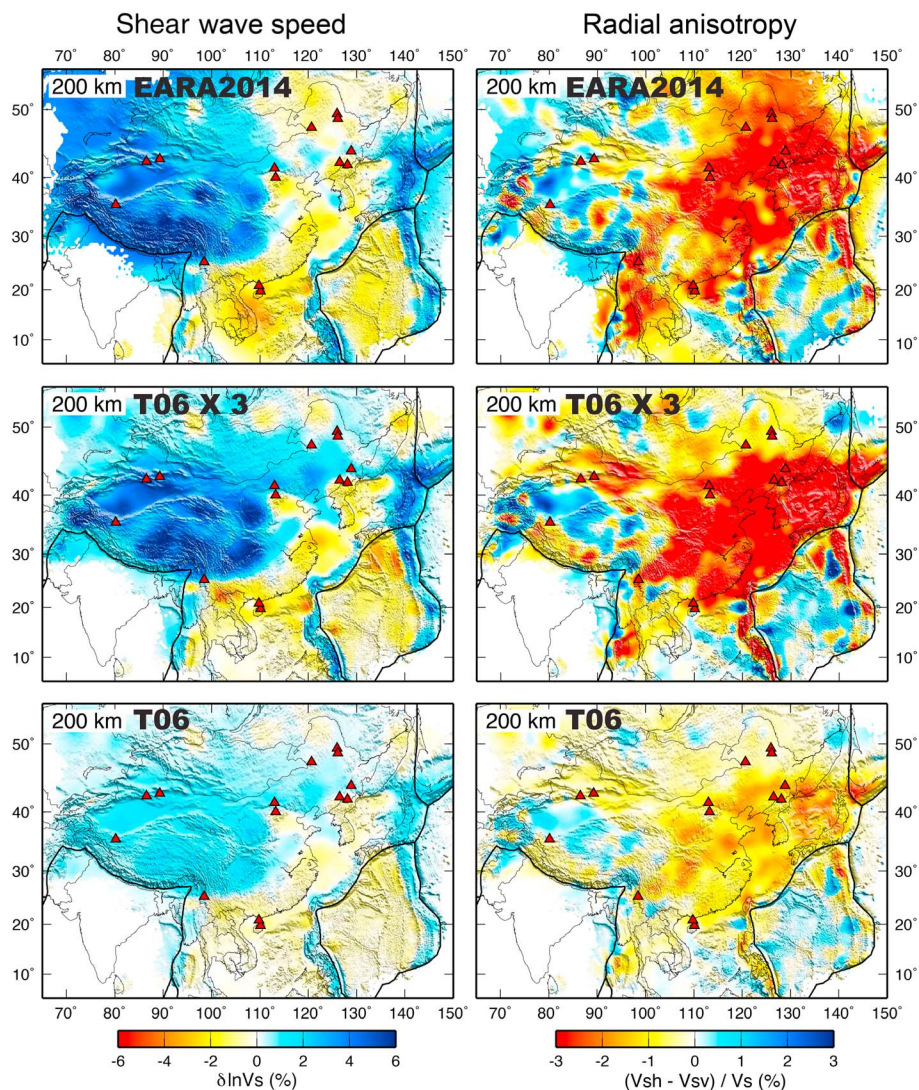


**Figure 12.** Comparison between (top row) EARA2014 and (bottom row) T06 at 200 km depth. T06 is inverted with a new starting model obtained by replacing EARA2014 by 1-D model STW105 between depths of 100 km and 300 km (the rest of the new starting model is the same as EARA2014). Maps of shear wave speed anomalies are shown on the left, and maps of radial anisotropy on the right. Middle row shows maps of T06 with shear wave speed anomalies and radial anisotropy amplified by a factor of 3, to compensate for the small number of iterations involved in the construction of T06.

beneath the Tibetan Plateau at the top of the mantle transition zone and in the uppermost mantle (Figures S10g and S10h). Tradeoffs between  $V_{SV}$  and  $V_{SH}$  or  $V_C$  are negligible in these regions, given the  $V_{SH}$  or  $V_C$  Hessian kernel maps appear to have zero amplitude, which gives confidence in future interpretation of radial anisotropy and  $V_P/V_S$  ratios.

### 3.5. Test With a Different Initial Model

At depths of 150 km, 200 km, and 250 km, the large-scale high-V beneath central and western China and low-V beneath eastern China do not change much from the S362ANI starting model, although short-wavelength variations (Figure 8), including narrow high-V slabs, do emerge from the smooth starting model (Figure S11). Thus, the question arises whether EARA2014 is robustly constrained by our data set in this depth range. In order to answer this question, we restart the adjoint inversion with a different initial model in which EARA2014 is replaced by 1-D model STW105 [Kustowski *et al.*, 2008a] between 100 km and 300 km depth; the rest of the model remains the same as EARA2014. After six iterations, model T06 (Figure 12) reassuringly shows shear wave speed anomalies and radial anisotropy patterns very similar to EARA2014 in the 100 km to 300 km depth range.

The results of this test indicate that long-wavelength wave speed and anisotropy patterns are robustly constrained by our data set in this depth range. Especially the positive radial anisotropy across eastern China at 200 km depth seems to be preferred by our data set. However, the amplitudes of the wave speed anomalies and radial anisotropy are reduced by roughly a third compared to EARA2014. This may reflect an insufficient number of tomographic iterations in the adjoint inversion, or convergence to a local minimum due to an improper starting model.

#### 4. Results and Discussions

Isotropic  $V_S$  and  $V_P$  anomalies and radial anisotropy  $\xi = (V_{SH} - V_{SV})/V_S$  are shown in maps at constant depth (Figures 8, 10, and 11). All maps are also plotted for the initial model for comparison (Figures S11, S12, and 11). The isotropic  $V_S$  and  $V_P$  images (Figures 8 and 10) generally agree in terms of wave speed anomaly patterns, but EARA2014-S (Figures 8) involves much sharper images of slabs and wave speed contrasts across the main tectonic boundaries, primarily due to the higher shear wave speed sensitivity of traveltimes. Therefore, we focus on describing the  $V_S$  model.

##### 4.1. Map Views of Isotropic $V_S$ and $V_P$ Anomalies

Quite a few features in EARA2014 (Figures 8 and 10) are consistent with previous tomographic results [Huang and Zhao, 2006; Li and van der Hilst, 2010; Obayashi et al., 2013; Schaeffer and Lebedev, 2013]. High-V anomalies beneath the Ordos Block and the Yangtze Platform indicate cold stable cratonic roots extending down to depths of about 250 km–300 km. Narrow high-V ( $V_P$  and  $V_S$ ) slabs appear from a depth of 100 km to the top of the mantle transition zone (depth of 400 km), following the trenches of Burma, Andaman, Kuril, Japan, Izu-Bonin, Mariana, Yap, Ryukyu, Malina, and the Philippines. Stagnant slabs reside inside the mantle transition zone (depths of 500 km and 600 km) beneath eastern China (east of 100°E) and are fragmented into different high-V zones, possibly corresponding to different episodes of slab subduction and retreat since the late Mesozoic [Fukao et al., 2001; Honza and Fujioka, 2004; Li and van der Hilst, 2010]. Alternatively, high-V anomalies observed inside the mantle transition zone beneath the Yangtze Platform could be lithosphere left by the collision between the South and North China Blocks [Lebedev and Nolet, 2003], and the high-V anomalies under the central and eastern North China Blocks are likely fossil lithosphere delaminated during an early Cretaceous giant igneous event [Wu et al., 2005; Yang et al., 2008]. High-V anomalies below the mantle transition zone (depths of 700 km and 900 km) imply that ancient oceanic or continental lithosphere penetrated the 650 km discontinuity and sank into the lower mantle beneath the North China Block, the Chuandian Block, the Northeast China Block, and the Ryukyu, Izu-Bonin, and Mariana Trenches. Broad low-V zones persist to a depth of 300 km beneath four regions, namely, the South China Sea, the Okinawa Trough, the West Philippine Basin, and the region to the east of Lake Baikal. These regions are possibly associated with slab subduction and stagnation or plume-induced upwellings. Moderate low-V zones appear in the lower mantle at a depth of 700 km beneath both the Japan Sea and the South China Sea, suggesting a possible lower mantle plume contribution to volcanism at Changbai and Hainan [Lebedev and Nolet, 2003; Montelli et al., 2004].

The main characteristics of EARA2014 include highly improved image clarity, especially in the crust and uppermost mantle (the uppermost 100 km), and newly imaged strong wave speed anomalies. At a depth of 50 km (Figure 8), the sharp transition from high-V (> 5%) to low-V (< -5%) anomalies clearly marks tectonic boundaries between the Nanshan Basin and the Altay-Sayan Mountain Range, the Tarim Basin and the Songpan Ganzi Fold Belt, and the Sichuan Basin and the Chuandian Block. At a depth of 100 km (Figure 8), high-V (> 3%) regions perfectly capture the shapes of the Tarim Basin, the Ordos Block, and the Yangtze Platform. From a depth of 150 km to the top of the transition zone, narrow slabs are crisply and continuously defined by higher than 1.5%  $V_S$  anomalies, in particular, for the relatively colder and younger Japan and Izu-Bonin slabs, which are defined by higher than 3%  $V_S$  anomalies.

There are several strong wave speed anomalies in EARA2014 images associated with tectonic features (Figure 8): (1) strong low-V zones with lower than -5%  $V_S$  anomalies coincident with long and narrow back-arc basins of convergent plate margins in the uppermost 100 km (depths of 20 km and 50 km), possibly associated with magma genesis from subduction-driven mantle flow, decompression melting, and slab dehydration [Pearce and Stern, 2006]; (2) a strong low-V zone correlated with the Altay-Sayan Mountain Range persists from

the crust to the uppermost mantle (depths of 20 km, 50 km, and 100 km), likely affected by an underlying mantle plume or asthenospheric diapir [Cunningham, 1998]; (3) strong low-V zones (lower than  $-5\%$   $V_S$  anomalies) exist beneath the northern Qiangtang Block [Brandon and Romanowicz, 1986; Bourjot and Romanowicz, 1992], the Songpan Ganzi Fold Belt, the Qilian Fold, and the Chuandian Block in the mid to lower crust (depths of 20 km and 50 km), which may support the existence of partial melt and/or aqueous fluid beneath the Tibetan Plateau [Yao et al., 2008; Caldwell et al., 2009; Bai et al., 2010; Chen et al., 2014]; (4) in the crust and uppermost mantle (depths of 20 km and 50 km), high-V anomalies correspond to the East Gobi and Erlian Basins right next to each other, the Songliao Basin in northeastern China, and low-V anomalies mark the Great Xing'an Range in between; (5) beneath the Tibetan Plateau, across the Lhasa and Qiangtang Block, a broad subvertical north dipping high-V structure (higher than 1.5 % in both  $V_P$  and  $V_S$ ; Figures 8 and 9) extends down to the bottom of the mantle transition zone (depths of 150 km–650 km), consistent at long-wavelength with the high-V anomalies in the latest global model SL2013sv [Schaeffer and Lebedev, 2013] (Figure 7) but missing in many other tomographic images [Huang and Zhao, 2006; Li and van der Hilst, 2010; Obrebski et al., 2012; Wei et al., 2012; Obayashi et al., 2013].

#### 4.2. Map Views of Radial Anisotropy

Radial anisotropy, i.e.,  $\xi = (V_{SH} - V_{SV})/V_S$ , is frequently determined from surface wave dispersion and is usually explained in terms of transverse isotropy with a vertical symmetry axis. It is a good indicator of lithospheric deformation in the crust and mantle, or mantle flow in the asthenosphere in either the vertical direction (negative  $\xi$ ) or horizontal direction (positive  $\xi$ ). Our inversion parameterizes radial anisotropy beneath the Moho and above 650 km (the bottom of the mantle transition zone), because complex crustal structure can introduce a strong trade-off between anisotropy and heterogeneity, and lower mantle radial anisotropy is not well constrained by our regional data set. It should be noted that the seismic waves we used to constrain radial anisotropy include not only surface waves but also all available body waves traveling in the upper mantle, especially  $P_n$ ,  $S_n$ ,  $PP$ , and  $SS$ . These complementary body waves increase the spatial resolution of radial anisotropy. Of course, there are other anisotropic parameters besides the five Love parameters that control wave propagation, for example,  $J_C$ ,  $J_S$ ,  $G_C$ , and  $G_S$  [Montagner and Nataf, 1986; Chen and Tromp, 2007]. We assume that the five Love parameters [Love, 1927] dominate wave propagation and provide a simple indicator of large-scale tectonic deformation styles, in particular, vertically or horizontally dominated flow. Future studies may focus on other elastic parameters given sufficient data coverage [Sieminski et al., 2007a, 2007b, 2009; Zhu and Tromp, 2013].

At a depth of 100 km (Figure 11), radial anisotropy  $\xi$  is qualitatively anticorrelated with  $V_S$  anomalies (Figure 8) in most regions of East Asia, except the east Tarim Basin, the north Ordos Block, and parts of the back-arc basins in the marginal seas of Japan, eastern China, and southern China. Low-V regions are dominated by positive radial anisotropy ( $\xi$  higher than 3 %) beneath the Tibetan Plateau, the Altay-Sayan Mountain Range, part of the Nanshan Basin, the northern Ordos Block, the Xing'an-East Mongolia Block, the Northeast China Block, and the Philippine Sea Plate. Narrow zones of negative  $\xi$  ( $< -3\%$ ) are mainly associated with arcs and back-arc basins. Medium to weakly negative  $\xi$  corresponds to high-V stable cratons, such as the Yangtze Platform, the western Tarim Basin, as well as the eastern part of the North China Block.

At a depth of 200 km (Figure 12), anticorrelation between radial anisotropy and  $V_S$  anomalies is not obvious, except along major arcs. Such a change in radial anisotropy relative to  $V_S$  anomalies in the 100 km to 200 km depth range could indicate a compositional transition from lithospheric to asthenospheric mantle (or vice versa), or a change in mantle flow modulated by lithosphere root architecture. Strong negative radial anisotropy ( $\xi < -3\%$ ) mostly exists beneath the marginal seas, eastern China, southeastern Tibet, Burma, and West and South Yunnan. Medium to weakly positive radial anisotropy occurs beneath the Philippine Sea Plate, western China, and Mongolia. Negative radial anisotropy associated with arcs and back arcs persists at 200 km depth.

Most of the strongly positive radial anisotropy ( $\xi > 3\%$ ) in EARA2014 (Figure 11) is limited to the upper 150 km of the mantle and coincides with the depth range of a hypothetical shear zone between the lithosphere and asthenosphere, where the preferred orientation of the olivine fast axis is horizontal [Ribe, 1989]. Negative radial anisotropy ( $\xi < -1.5\%$ ) generally correlates with intraplate volcanoes at depths deeper than 150 km (Figure 12), such as the Wudalianchi, Changbai, Hainan, Tengchong, and Arshan volcanoes. Negative radial anisotropy ( $\xi < -1.5\%$ ) also occurs in subduction zones within both the slab and the mantle wedge (Figures 11 and 12). However, radial anisotropy in these two regions can be caused by different mechanisms. We speculate

that there are different origins of strong negative radial anisotropy in the mantle wedge above the slab versus within the slab. Atop of the subducting slab, mantle downwelling due to the drag force of the subducting slab induces large strain enabling perfect downdip alignment of olivine crystals. Thus, negative radial anisotropy in the mantle wedge (Figures 11 and 12) is possibly a manifestation of flow-oriented olivine. In contrast, radial anisotropy within the slab (Figures 11 and 12) may represent extrinsic anisotropy, for example, an equivalent apparent negative radial anisotropy induced by fine planar layering inside the slab oriented subvertically [Wang *et al.*, 2013]. We confirm subduction zone radial anisotropy reported in previous studies [Panning and Romanowicz, 2006; Yeh *et al.*, 2013] but provide much higher resolution images that start to reveal a link between the mantle dynamics and radial anisotropy.

## 5. Conclusions

We present a new 3-D radially anisotropic seismic model of East Asia, named EARA2014, based on adjoint tomography. This paper focuses on technical aspects of constructing the model and provides a general discussion by comparing  $V_{SV}$ , isotropic  $V_S$  and  $V_P$ , and radial anisotropy images of EARA2014 with other models. Wave speed anomalies in EARA2014 are highly localized within known tectonic units and show very sharp contrasts across tectonic boundaries in the uppermost 100 km. We observe a broad high-V structure beneath Tibet (higher than 1.5 % in both  $V_P$  and  $V_S$ ), spanning across the Lhasa and Qiangtang Block, and extending from below 100 km depth to the bottom of the mantle transition zone. Detailed interpretations of certain tectonic features, such as the Tibetan Plateau and the Altay-Sayan Mountain Range, with additional constraints from radial anisotropy and the  $V_P/V_S$  ratio, will be presented in a separate paper.

Future inversions using this data set will focus on 3-D variations in azimuthal anisotropy and attenuation beneath East Asia.

## Acknowledgments

We thank the Editor (Robert Nowack), the Associate Editor, Reviewer 1 (anonymous), and Reviewer 2 (Barbara Romanowicz) for their constructive comments that helped improve the manuscript. We also thank Bogdan Kustowski, Andrew Schaeffer, Mathias Obrebski, Masayuki Obayashi, and Yingjie Yang for making their models available in digital format. We appreciate valuable discussions with Hejun Zhu, Yang Luo, Ebru Bozdağ, and Andreas Fichtner on adjoint tomography. We thank the various networks that contributed data, as well as the Rice Research Computing Support Group. The majority of waveform data were provided by the China Seismic Array Data Management Center at the Institute of Geophysics, China Earthquake Administration. Data and synthetics processing was accomplished based on the Seismic Analysis Code (SAC). All maps and cross sections were made with the Generic Mapping Tool (GMT). The open source spectral-element software package SPECFEM3D GLOBE, the seismic measurement software package FLEXTWIN, and moment tensor inversion package CMT3D used for this article are freely available for download via the Computational Infrastructure for Geodynamics (CIG; [geodynamics.org](http://geodynamics.org)). This research was supported by XSEDE research allocation TG-EAR130011 and NSF grants 1063057, 1112906, and 1345096.

## References

- Agius, M. R., and S. Lebedev (2013), Tibetan and Indian lithospheres in the upper mantle beneath Tibet: Evidence from broadband surface-wave dispersion, *Geochem. Geophys. Geosyst.*, 14, 4260–4281, doi:10.1002/ggpe.20274.
- Allégre, C. J., *et al.* (1984), Structure and evolution of the Himalaya–Tibet orogenic belt, *Nature*, 307, 17–22.
- Anderson, D. L. (1987), A seismic equation of state II. Shear properties and thermodynamics of the lower mantle, *Phys. Earth Planet. Inter.*, 45, 307–323.
- Anderson, D. L. (2005), Large igneous provinces, delamination, and fertile mantle, *Elements*, 1(5), 271–275, doi:10.2113/gselements.1.5.271.
- Auer, L., L. Boschi, T. W. Becker, and D. Giardini (2014), Savani: A variable resolution whole-mantle model of anisotropic shear velocity variations based on multiple data sets, *J. Geophys. Res. Solid Earth*, 119, 3006–3034, doi:10.1002/2013JB010773.
- Bai, D., *et al.* (2010), Crustal deformation of the eastern Tibetan plateau revealed by magnetotelluric imaging, *Nat. Geosci.*, 3(5), 358–362, doi:10.1038/ngeo830.
- Barry, T. L., A. D. Saunders, P. D. Kempton, B. F. Windley, M. S. Pringle, D. Dorjnamjaa, and S. Saandar (2003), Petrogenesis of Cenozoic basalts from Mongolia: Evidence for the role of asthenospheric versus metasomatized lithospheric mantle sources, *J. Petrol.*, 44(1), 55–91.
- Bassin, C., G. Laske, and G. Masters (2000), The current limits of resolution for surface wave tomography in North America, *Eos. Trans. AGU*, 81, F897.
- Bodin, T., Y. Capdeville, B. Romanowicz, and J. Montagner (2015), Interpreting radial anisotropy in global and regional tomographic models, in *The Earth's Heterogeneous Mantle*, edited by A. Khan, F. Deschamps, and K. Kawai, Springer.
- Bourjot, L., and B. Romanowicz (1992), Crust and upper mantle tomography in Tibet using surface waves, *Geophys. Res. Lett.*, 19(9), 881–884, doi:10.1029/92GL00261.
- Brandon, C., and B. Romanowicz (1986), A “no-lid” zone in the central Chang-Thang platform of Tibet: Evidence from pure path phase velocity measurements of long period Rayleigh waves, *J. Geophys. Res.*, 91(B6), 6547–6564, doi:10.1029/JB091iB06p06547.
- Burchfiel, B. C., and L. H. Royden (1991), Tectonics of Asia 50 years after the death of Emile Argand, *Eclogae Geol. Helv.*, 599–629.
- Caldwell, W. B., S. L. Klemperer, S. S. Rai, and J. F. Lawrence (2009), Partial melt in the upper-middle crust of the northwest Himalaya revealed by Rayleigh wave dispersion, *Tectonophysics*, 477, 58–65, doi:10.1016/j.tecto.2009.01.013.
- Chen, M., and J. Tromp (2007), Theoretical and numerical investigations of global and regional seismic wave propagation in weakly anisotropic earth models, *Geophys. J. Int.*, 168(3), 1130–1152, doi:10.1111/j.1365-246X.2006.03218.x.
- Chen, M., H. Huang, H. Yao, R. D. van der Hilst, and F. Niu (2014), Low wave speed zones in the crust beneath SE Tibet revealed by ambient noise adjoint tomography, *Geophys. Res. Lett.*, 41, 334–340, doi:10.1002/2013GL058476.
- Chen, P., L. Zhao, and T. H. Jordan (2007), Full 3D tomography for the crustal structure of the Los Angeles region, *Bull. Seismol. Soc. Am.*, 97(4), 1094–1120, doi:10.1785/0120060222.
- Chen, Y., J. Badal, and Z. Zhang (2009), Radial anisotropy in the crust and upper mantle beneath the Qinghai-Tibet Plateau and surrounding regions, *J. Asian Earth Sci.*, 36, 289–302, doi:10.1016/j.jseaes.2009.06.011.
- Cunningham, W. D. (1998), Lithospheric controls on late Cenozoic construction of the Mongolian Altai, *Tectonics*, 17(6), 891–902, doi:10.1029/1998TC900001.
- Cunningham, W. D. (2001), Cenozoic normal faulting and regional doming in the southern Hangay region, Central Mongolia: implications for the origin of the Baikal rift province, *Tectonophysics*, 337, 389–411, doi:10.1016/S0040-1951(00)00228-6.
- DeMets, C., R. G. Gordon, D. F. Argus, and S. Stein (1990), Current plate motions, *Geophys. J. Int.*, 101, 425–478.
- Dewey, J. F., S. Cande, and W. C. Pitman (1989), Tectonic evolution of the India/Eurasia Collision Zone, *Eclogae Geol. Helv.*, 82(3), 717–734.
- Ekström, G., A. M. Dziewoński, N. N. Maternovskaya, and M. Nettles (2005), Global seismicity of 2003: Centroid–moment-tensor solutions for 1087 earthquakes, *Phys. Earth Planet. Inter.*, 148(2–4), 327–351, doi:10.1016/j.pepi.2004.09.006.

- Faccenna, C., T. W. Becker, S. Lallemand, Y. Lagabrielle, F. Funiciello, and C. Piromallo (2010), Subduction-triggered magmatic pulses: A new class of plumes?, *Earth Planet. Sci. Lett.*, 299, 54–68, doi:10.1016/j.epsl.2010.08.012.
- Fichtner, A., and J. Trampert (2011a), Hessian kernels of seismic data functionals based upon adjoint techniques, *Geophys. J. Int.*, 185(2), 775–798, doi:10.1111/j.1365-246X.2011.04966.x.
- Fichtner, A., and J. Trampert (2011b), Resolution analysis in full waveform inversion, *Geophys. J. Int.*, 187(3), 1604–1624, doi:10.1111/j.1365-246X.2011.05218.x.
- Fichtner, A., B. L. N. Kennett, H. Igel, and H.-P. Bunge (2009), Full seismic waveform tomography for upper-mantle structure in the Australasian region using adjoint methods, *Geophys. J. Int.*, 179(3), 1703–1725, doi:10.1111/j.1365-246X.2009.04368.x.
- Fichtner, A., B. L. N. Kennett, H. Igel, and H.-P. Bunge (2010), Full waveform tomography for radially anisotropic structure: New insights into present and past states of the Australasian upper mantle, *Earth Planet. Sci. Lett.*, 290(3–4), 270–280, doi:10.1016/j.epsl.2009.12.003.
- French, S., V. Lekic, and B. Romanowicz (2013), Waveform tomography reveals channeled flow at the base of the oceanic asthenosphere, *Science*, 342, 227–230, doi:10.1126/science.1241514.
- French, S. W., and B. A. Romanowicz (2014), Whole-mantle radially anisotropic shear velocity structure from spectral-element waveform tomography, *Geophys. J. Int.*, 199, 1303–1327, doi:10.1093/gji/ggu334.
- Friederich, W. (2003), The S-velocity structure of the East Asian mantle from inversion of shear and surface waveforms, *Geophys. J. Int.*, 153, 88–102.
- Fukao, Y., S. Widjiantoro, and M. Obayashi (2001), Stagnant slabs in the upper and lower mantle transition region, *Rev. Geophys.*, 39, 291–323, doi:10.1029/1999RG000068.
- Hjörleifsdóttir, V., and G. Ekström (2010), Effects of three-dimensional Earth structure on CMT earthquake parameters, *Phys. Earth Planet. Inter.*, 179(3–4), 178–190, doi:10.1016/j.pepi.2009.11.003.
- Honza, E., and K. Fujioka (2004), Formation of arcs and backarc basins inferred from the tectonic evolution of Southeast Asia since the Late Cretaceous, *Tectonophysics*, 384(1–4), 23–53, doi:10.1016/j.tecto.2004.02.006.
- Huang, J., and D. Zhao (2006), High-resolution mantle tomography of China and surrounding regions, *J. Geophys. Res.*, 111, B09305, doi:10.1029/2005JB004066.
- Hunt, A. C., I. J. Parkinson, N. B. W. Harris, T. L. Barry, N. W. Rogers, and M. Yondon (2012), Cenozoic volcanism on the Hangai Dome, Central Mongolia: Geochemical evidence for changing melt sources and implications for mechanisms of melting, *J. Petrol.*, 53(9), 1913–1942, doi:10.1093/petrology/egs038.
- Khai, V. E. (1990), Origin of the Central Asian mountain belt: Collision or mantle diapirism, *J. Geodyn.*, 11, 389–394.
- Komatitsch, D., and J. Tromp (2002a), Spectral-element simulations of global seismic wave propagation—I. Validation, *Geophys. J. Int.*, 149, 390–412, doi:10.1046/j.1365-246X.2002.01653.x.
- Komatitsch, D., and J. Tromp (2002b), Spectral-element simulations of global seismic wave propagation—II. Three-dimensional models, oceans, rotation and self-gravitation, *Geophys. J. Int.*, 150, 303–318, doi:10.1046/j.1365-246X.2002.01716.x.
- Kustowski, B., G. Ekström, and A. M. Dziewoński (2008a), Anisotropic shear-wave velocity structure of the Earth's mantle: A global model, *J. Geophys. Res.*, 113, 1–23, doi:10.1029/2007JB005169.
- Kustowski, B., G. Ekström, and A. M. Dziewoński (2008b), The shear-wave velocity structure in the upper mantle beneath Eurasia, *Geophys. J. Int.*, 174, 978–992, doi:10.1111/j.1365-246X.2008.03865.x.
- Lebedev, S., and G. Nolet (2003), Upper mantle beneath Southeast Asia from S velocity tomography, *J. Geophys. Res.*, 108(B1), 2048, doi:10.1029/2000JB000073.
- Lebedev, S., and R. D. van der Hilst (2008), Global upper-mantle tomography with the automated multimode inversion of surface and S-wave forms, *Geophys. J. Int.*, 173(2), 505–518, doi:10.1111/j.1365-246X.2008.03721.x.
- Lebedev, S., J. Boonen, and J. Trampert (2009), Seismic structure of Precambrian lithosphere: New constraints from broad-band surface-wave dispersion, *Lithos*, 109, 96–111, doi:10.1016/j.lithos.2008.06.010.
- Lei, J., and D. Zhao (2005), P-wave tomography and origin of the Changbai intraplate volcano in Northeast Asia, *Tectonophysics*, 397, 281–295, doi:10.1016/j.tecto.2004.12.009.
- Lévéque, J., L. Rivera, and G. Wittlinger (1993), On the use of the checker-board test to assess the resolution of tomographic inversions, *Geophys. J. Int.*, 313–318, doi:10.1111/j.1365-246X.1993.tb05605.x.
- Li, C., and R. D. van der Hilst (2010), Structure of the upper mantle and transition zone beneath Southeast Asia from travelttime tomography, *J. Geophys. Res.*, 115, B07308, doi:10.1029/2009JB006882.
- Li, C., R. D. van der Hilst, A. S. Meltzer, and E. R. Engdahl (2008), Subduction of the Indian lithosphere beneath the Tibetan Plateau and Burma, *Earth Planet. Sci. Lett.*, 274, 157–168, doi:10.1016/j.epsl.2008.07.016.
- Liu, Q., and J. Tromp (2006), Finite-frequency kernels based on adjoint methods, *Bull. Seismol. Soc. Am.*, 96(6), 2383–2397, doi:10.1785/0120060041.
- Liu, Q., and J. Tromp (2008), Finite-frequency sensitivity kernels for global seismic wave propagation based upon adjoint methods, *Geophys. J. Int.*, 174(1), 265–286, doi:10.1111/j.1365-246X.2008.03798.x.
- Liu, Q., J. Polet, D. Komatitsch, and J. Tromp (2004), Spectral-element moment tensor inversions for earthquakes in Southern California, *Bull. Seismol. Soc. Am.*, 94(5), 1748–1761, doi:10.1785/012004038.
- Love, A. E. H. (1927), *A Treatise on the Mathematical Theory of Elasticity*, Cambridge Univ. Press, Cambridge, U. K.
- Luo, Y., R. Modrak, and J. Tromp (2013), Strategies in Adjoint Tomography, in *Handbook of Geomathematics*, 2nd ed., edited by W. Freeden, Z. Nahed, and T. Sonar, Springer.
- Maggi, A., C. Tape, M. Chen, D. Chao, and J. Tromp (2009), An automated time-window selection algorithm for seismic tomography, *Geophys. J. Int.*, 178(1), 257–281, doi:10.1111/j.1365-246X.2009.04099.x.
- Montagner, J., and H. Nataf (1986), A simple method for inverting the azimuthal anisotropy of surface waves, *J. Geophys. Res.*, 91(B1), 511–520, doi:10.1029/JB091iB01p00511.
- Montelli, R., G. Nolet, F. A. Dahlen, G. Masters, E. R. Engdahl, and S.-H. Hung (2004), Finite-frequency tomography reveals a variety of plumes in the mantle, *Science*, 303(5656), 338–343, doi:10.1126/science.1092485.
- National Geophysical Data Center (2006), 2-minute gridded global relief data (ETOPO2v2), *World Data Serv. Geophys. U.S. Dep. Commer.*, NOAA, Boulder, Colo. [Available at <http://www.ngdc.noaa.gov/mgg/fliers/06mgg01.html>.]
- Northrup, C. J., L. H. Royden, and B. C. Burchfiel (1995), Motion of the Pacific plate relative to Eurasia and its potential relation to Cenozoic extension along the eastern margin of Eurasia, *Geology*, 23(8), 719–722, doi:10.1130/0091-7613(1995)023<0719:MOPTPR>2.3.CO;2.
- Obayashi, M., J. Yoshimitsu, G. Nolet, Y. Fukao, H. Shiobara, H. Sugioka, H. Miyamachi, and Y. Gao (2013), Finite frequency whole mantle P wave tomography: Improvement of subducted slab images, *Geophys. Res. Lett.*, 40, 5652–5657, doi:10.1002/2013GL057401.
- Obrebski, M., R. M. Allen, F. Zhang, J. Pan, Q. Wu, and S.-H. Hung (2012), Shear wave tomography of China using joint inversion of body and surface wave constraints, *J. Geophys. Res.*, 117, 1–15, doi:10.1029/2011JB008349.

- Panning, M., and B. Romanowicz (2006), A three-dimensional radially anisotropic model of shear velocity in the whole mantle, *Geophys. J. Int.*, 167(1), 361–379, doi:10.1111/j.1365-246X.2006.03100.x.
- Panning, M. P., V. Lekić, and B. A. Romanowicz (2010), Importance of crustal corrections in the development of a new global model of radial anisotropy, *J. Geophys. Res.*, 115, B12325, doi:10.1029/2010JB007520.
- Panning, M. P., A. Cao, A. Kim, and B. A. Romanowicz (2012), Non-linear 3-D Born shear waveform tomography in Southeast Asia, *Geophys. J. Int.*, 190, 463–475, doi:10.1111/j.1365-246X.2012.05489.x.
- Pearce, J. A., and R. J. Stern (2006), Origin of back-arc basin magmas: Trace element and isotope perspectives, *Back-Arc Spreading Syst. Geol. Biol. Chem. Phys. Interact. Geophys. Monogr. Ser.* 166.
- Petit, C., J. De, and D. Fairhead (2002), Deep structure and mechanical behavior of the lithosphere in the Hangai-Hövsgöl region, Mongolia: New constraints from gravity modeling, *Earth Planet. Sci. Lett.*, 197, 133–149.
- Priestley, K., and D. Mckenzie (2006), The thermal structure of the lithosphere from shear wave velocities, *Earth Planet. Sci. Lett.*, 244(1–2), 285–301, doi:10.1016/j.epsl.2006.01.008.
- Priestley, K., E. Debayle, D. Mckenzie, and S. Pilidou (2006), Upper mantle structure of eastern Asia from multimode surface waveform tomography, *J. Geophys. Res.*, 111, B10304, doi:10.1029/2005JB004082.
- Qin, Y., Y. Capdeville, V. Maupin, J.-P. Montagner, S. Lebedev, and E. Beucler (2008), SPICE benchmark for global tomographic methods, *Geophys. J. Int.*, 175(2), 598–616, doi:10.1111/j.1365-246X.2008.03904.x.
- Ren, J., K. Tamaki, S. Li, and Z. Junxia (2002), Late Mesozoic and Cenozoic rifting and its dynamic setting in Eastern China and adjacent areas, *Tectonophysics*, 344(3–4), 175–205, doi:10.1016/S0040-1951(01)00271-2.
- Ribe, N. M. (1989), Seismic anisotropy and mantle flow, *J. Geophys. Res.*, 94(88), 4213–4223, doi:10.1029/JB094iB04p04213.
- Schaeffer, A. J., and S. Lebedev (2013), Global shear speed structure of the upper mantle and transition zone, *Geophys. J. Int.*, doi:10.1093/gji/ggt095.
- Schellart, W. P., and G. S. Lister (2005), The role of the East Asian active margin in widespread extensional and strike-slip deformation in East Asia, *J. Geol. Soc. London*, 162, 959–972.
- Sieminski, A., Q. Liu, J. Trampert, and J. Tromp (2007a), Finite-frequency sensitivity of body waves to anisotropy based upon adjoint methods, *Geophys. J. Int.*, 171(1), 368–389, doi:10.1111/j.1365-246X.2007.03528.x.
- Sieminski, A., Q. Liu, J. Trampert, and J. Tromp (2007b), Finite-frequency sensitivity of surface waves to anisotropy based upon adjoint methods, *Geophys. J. Int.*, 168(3), 1153–1174, doi:10.1111/j.1365-246X.2006.03261.x.
- Sieminski, A., J. Trampert, and J. Tromp (2009), Principal component analysis of anisotropic finite-frequency sensitivity kernels, *Geophys. J. Int.*, 179(2), 1186–1198, doi:10.1111/j.1365-246X.2009.04341.x.
- Tang, Y., M. Obayashi, F. Niu, S. P. Grand, Y. J. Chen, H. Kawakatsu, S. Tanaka, J. Ning, and J. F. Ni (2014), Changbaishan volcanism in northeast China linked to subduction-induced mantle upwelling, *Nat. Geosci.*, 7(6), 470–475, doi:10.1038/ngeo2166.
- Tape, C., Q. Liu, and J. Tromp (2007), Finite-frequency tomography using adjoint methods—Methodology and examples using membrane surface waves, *Geophys. J. Int.*, 168(3), 1105–1129, doi:10.1111/j.1365-246X.2006.03191.x.
- Tape, C., Q. Liu, A. Maggi, and J. Tromp (2009), Adjoint tomography of the southern California crust, *Science*, 325, 988–992, doi:10.1126/science.1175298.
- Tape, C., Q. Liu, A. Maggi, and J. Tromp (2010), Seismic tomography of the southern California crust based on spectral-element and adjoint methods, *Geophys. J. Int.*, 180(1), 433–462, doi:10.1111/j.1365-246X.2009.04429.x.
- Tappognier, P., G. Peltzer, and R. Armijo (1986), On the mechanics of the collision between India and Asia, *Geol. Soc. London Spec. Publ.*, 19(1), 113–157, doi:10.1144/GSL.SP.1986.019.01.07.
- Tiberi, C., A. Deschamps, J. Déverchère, C. Petit, J. Perrot, D. Appriou, V. Mordvinova, T. Dugaarma, M. Ulzibaat, and A. A. Artemiev (2008), Asthenospheric imprints on the lithosphere in Central Mongolia and Southern Siberia from a joint inversion of gravity and seismology (MOBAL experiment), *Geophys. J. Int.*, 175(3), 1283–1297, doi:10.1111/j.1365-246X.2008.03947.x.
- Tilmann, F., J. Ni, and I. I. S. Team (2003), Seismic Imaging of the Downwelling Indian Lithosphere Beneath Central Tibet, *Science*, 300(1424), doi:10.1126/science.1082777.
- Tromp, J., C. Tape, and Q. Liu (2005), Seismic tomography, adjoint methods, time reversal and banana-doughnut kernels, *Geophys. J. Int.*, 160(1), 195–216, doi:10.1111/j.1365-246X.2004.02453.x.
- Wang, N., J.-P. Montagner, A. Fichtner, and Y. Capdeville (2013), Intrinsic versus extrinsic seismic anisotropy: The radial anisotropy in reference Earth models, *Geophys. Res. Lett.*, 40, 4284–4288, doi:10.1002/grl.50873.
- Watson, M. P., A. B. Hayward, D. N. Parkinson, and Z. M. Zhang (1987), Plate tectonic history, basin development and petroleum source rock deposition onshore China, *Mar. Petrol. Geol.*, 4, 205–225, doi:10.1016/0264-8172(87)90045-6.
- Wei, W., J. Xu, D. Zhao, and Y. Shi (2012), East Asia mantle tomography: New insight into plate subduction and intraplate volcanism, *J. Asian Earth Sci.*, 60, 88–103, doi:10.1016/j.jseas.2012.08.001.
- Windley, B. F., and M. B. Allen (1993), Mongolian plateau: Evidence for a late Cenozoic mantle plume under central Asia, *Geology*, doi:10.1130/0091-7613(1993)021<0295.
- Wu, F., J. Lin, S. Wilde, X. Zhang, and J. Yang (2005), Nature and significance of the Early Cretaceous giant igneous event in eastern China, *Earth Planet. Sci. Lett.*, 233(1–2), 103–119, doi:10.1016/j.epsl.2005.02.019.
- Yang, J.-H., F.-Y. Wu, S. A. Wilde, E. Belousova, and W. L. Griffin (2008), Mesozoic decratonization of the North China block, *Geology*, 36(6), 467, doi:10.1130/G24518A.1.
- Yang, Y., M. H. Ritzwoller, Y. Zheng, W. Shen, A. L. Levshin, and Z. Xie (2012), A synoptic view of the distribution and connectivity of the mid-crustal low velocity zone beneath Tibet, *J. Geophys. Res.*, 117, B04303, doi:10.1029/2011JB008810.
- Yao, H., C. Beghein, and R. D. van der Hilst (2008), Surface wave array tomography in SE Tibet from ambient seismic noise and two-station analysis—I. Crustal and upper-mantle structure, *Geophys. J. Int.*, 173(1), 205–219, doi:10.1111/j.1365-246X.2007.03696.x.
- Yao, H., R. D. van der Hilst, and J.-P. Montagner (2010), Heterogeneity and anisotropy of the lithosphere of SE Tibet from surface wave array tomography, *J. Geophys. Res.*, 115, B12307, doi:10.1029/2009JB007142.
- Yeh, Y.-L., H. Kao, S. Wen, W.-Y. Chang, and C.-H. Chen (2013), Surface wave tomography and azimuthal anisotropy of the Philippine Sea Plate, *Tectonophysics*, 592, 94–112, doi:10.1016/j.tecto.2013.02.005.
- Yin, A., and T. M. Harrison (2000), Geologic evolution of the Himalayan-Tibetan orogen, *Annu. Rev. Earth Planet. Sci.*, 28, 211–280, doi:10.1146/annurev.earth.28.1.211.
- Zhao, D., Y. Tian, J. Lei, L. Liu, and S. Zheng (2009), Seismic image and origin of the Changbai intraplate volcano in East Asia: Role of big mantle wedge above the stagnant Pacific slab, *Phys. Earth Planet. Inter.*, 173(3–4), 197–206, doi:10.1016/j.pepi.2008.11.009.
- Zhao, L., R. M. Allen, T. Zheng, and R. Zhu (2012), High-resolution body wave tomography models of the upper mantle beneath eastern China and the adjacent areas, *Geochem. Geophys. Geosyst.*, 13, Q06007, doi:10.1029/2012GC004119.

- Zheng, X., B. Ouyang, D. Zhang, Z. Yao, J. Liang, and J. Zheng (2009), Technical system construction of Data Backup Centre for China Seismograph Network and the data support to researches on the Wenchuan earthquake [in Chinese], *Chin. J. Geophys.*, 52(5), 1412–1417, doi:10.3969/j.issn.0001-5733.2009.05.031.
- Zhu, H., and J. Tromp (2013), Mapping tectonic deformation in the crust and upper mantle beneath Europe and the North Atlantic Ocean, *Science*, 341, 871–875, doi:10.1126/science.1241335.
- Zhu, H., E. Bozdağ, D. Peter, and J. Tromp (2012a), Seismic wavespeed images across the Iapetus and Tornquist suture zones, *Geophys. Res. Lett.*, 39, L18304, doi:10.1029/2012GL053053.
- Zhu, H., E. Bozdağ, D. Peter, and J. Tromp (2012b), Structure of the European upper mantle revealed by adjoint tomography, *Nat. Geosci.*, 5(7), 493–498, doi:10.1038/ngeo1501.
- Zhu, H., E. Bozdağ, T. S. Duffy, and J. Tromp (2013), Seismic attenuation beneath Europe and the North Atlantic: Implications for water in the mantle, *Earth Planet. Sci. Lett.*, 381, doi:10.1016/j.epsl.2013.08.030.
- Zorin, Y. A., E. K. Turutanov, V. M. Kozhevnikov, S. V. Rasskazov, and A. I. Ivanov (2006), The nature of Cenozoic upper mantle plumes in East Siberia (Russia) and Central Mongolia, *Russ. Geol. Geophys.*, 47(10), 1056–1070.